

1 **Development and evaluation of a variably saturated flow model in the global**
2 **E3SM Land Model (ELM) Version 1.0**

3

4 **Gautam Bisht¹, William J. Riley¹, Glenn E. Hammond², and David M. Lorenzetti³**

5

6 ¹Climate & Ecosystem Sciences Division, Lawrence Berkeley National Laboratory,1
7 Cyclotron Road, Berkeley, California 94720, USA

8

9 ²Applied Systems Analysis and Research Department, Sandia National Laboratories,
10 Albuquerque, NM 87185-0747, USA

11

12 ³Sustainable Energy Systems Group, Lawrence Berkeley National Laboratory,1
13 Cyclotron Road, Berkeley, California 94720, USA

14

15 Correspondence to: Gautam Bisht (gbisht@lbl.gov)

16 **Abstract**

17 Improving global-scale model representations of coupled surface and groundwater
18 hydrology is important for accurately simulating terrestrial processes and predicting
19 climate change effects on water resources. Most existing land surface models,
20 including the default E3SM Land Model (ELMv0), which we modify here, routinely
21 employ different formulations for water transport in the vadose and phreatic zones.
22 In this work, we developed the Variably Saturated Flow Model (VSFM) in ELMv1 to
23 unify the treatment of soil hydrologic processes in the unsaturated and saturated
24 zones. VSFM was tested on three benchmark problems and results were evaluated
25 against observations and an existing benchmark model (PFLOTRAN). The ELMv1-
26 VSFM's subsurface drainage parameter, f_d , was calibrated to match an
27 observationally-constrained and spatially-explicit global water table depth (WTD)
28 product. Optimal spatially-explicit f_d values were obtained for 79% of global $1.9^0 \times$
29 2.5^0 gridcells, while the remaining 21% of global gridcells had predicted WTD deeper
30 than the observationally-constrained estimate. Comparison with predictions using
31 the default f_d value demonstrated that calibration significantly improved predictions,
32 primarily by allowing much deeper WTDs. Model evaluation using the International
33 Land Model Benchmarking package (ILAMB) showed that improvements in WTD
34 predictions did not degrade model skill for any other metrics. We evaluated the
35 computational performance of the VSFM model and found that the model is about
36 30% more expensive than the default ELMv0 with an optimal processor layout. The
37 modular software design of VSFM not only provides flexibility to configure the model
38 for a range of problem setups, but also allows building the model independently of
39 the ELM code, thus enabling straightforward testing of model's physics against other
40 models.

41 **1 Introduction**

42 Groundwater, which accounts for 30% of freshwater reserves globally, is a vital
43 human water resource. It is estimated that groundwater provides 20-30% of global
44 freshwater withdrawals (Petra, 2009; Zektser and Evertt, 2004), and that irrigation
45 accounts for ~70% of these withdrawals (Siebert et al., 2010). Climate change is
46 expected to impact the quality and quantity of groundwater in the future (Alley,
47 2001). As temporal variability of precipitation and surface water increases in the
48 future due to climate change, reliance on groundwater as a source of fresh water for
49 domestic, agriculture, and industrial use is expected to increase (Taylor et al., 2013).

50 Local environmental conditions modulate the impact of rainfall changes on
51 groundwater resources. For example, high intensity precipitation in humid areas may
52 lead to a decrease in groundwater recharge (due to higher surface runoff), while arid
53 regions are expected to see gains in groundwater storage (as infiltrating water
54 quickly travels deep into the ground before it can be lost to the atmosphere)
55 (Kundzewicz and Doli, 2009). Although global climate models predict changes in
56 precipitation over the next century (Marvel et al., 2017), few global models that
57 participated in the recent Coupled Model Inter-comparison Project (CMIP5; Taylor et
58 al. (2012)) were able to represent global groundwater dynamics accurately (e.g.
59 Swenson and Lawrence (2014))

60 Modeling studies have also investigated impacts, at watershed to global scales,
61 on future groundwater resources associated with land-use (LU) and land-cover (LC)
62 change (Dams et al., 2008) and ground water pumping (Ferguson and Maxwell, 2012;
63 Leng et al., 2015). Dams et al. (2008) predicted that LU changes would result in a small
64 mean decrease in subsurface recharge and large spatial and temporal variability in
65 groundwater depth for the Kleine Nete basin in Belgium. Ferguson and Maxwell
66 (2012) concluded that groundwater-fed irrigation impacts on water exchanges with
67 the atmosphere and groundwater resources can be comparable to those from a 2.5 °C
68 increase in air temperature for the Little Washita basin in Oklahoma, USA. By
69 performing global simulations of climate change scenarios using CLM4, Leng et al.
70 (2015) concluded that the water source (i.e., surface or groundwater) used for

71 irrigation depletes the corresponding water source while increasing the storage of
72 the other water source. Recently, Leng et al. (2017) showed that irrigation method
73 (drip, sprinkler, or flood) has impacts on water balances and water use efficiency in
74 global simulations.

75 Groundwater models are critical for developing understanding of
76 groundwater systems and predicting impacts of climate (Green et al., 2011). Kollet
77 and Maxwell (2008) identified critical zones, i.e., regions within the watershed with
78 water table depths between 1 – 5 m, where the influence of groundwater dynamics
79 was largest on surface energy budgets. Numerical studies have demonstrated impacts
80 of groundwater dynamics on several key Earth system processes, including soil
81 moisture (Chen and Hu, 2004; Liang et al., 2003; Salvucci and Entekhabi, 1995; Yeh
82 and Eltahir, 2005), runoff generation (Levine and Salvucci, 1999; Maxwell and Miller,
83 2005; Salvucci and Entekhabi, 1995; Shen et al., 2013), surface energy budgets
84 (Alkhaier et al., 2012; Niu et al., 2017; Rihani et al., 2010; Soylu et al., 2011), land-
85 atmosphere interactions (Anyah et al., 2008; Jiang et al., 2009; Leung et al., 2011;
86 Yuan et al., 2008), vegetation dynamics (Banks et al., 2011; Chen et al., 2010), and soil
87 biogeochemistry (Lohse et al., 2009; Pacific et al., 2011).

88 Recognizing the importance of groundwater systems on terrestrial processes,
89 groundwater models of varying complexity have been implemented in land surface
90 models (LSMs) in recent years. Groundwater models in current LSMs can be classified
91 into four categories based on their governing equations. Type-1 models assume a
92 quasi-steady state equilibrium of the soil moisture profile above the water table
93 (Hilberts et al., 2005; Koster et al., 2000; Walko et al., 2000). Type-2 models use a θ -
94 based (where θ is the water volume content) Richards equation in the unsaturated
95 zone coupled with a lumped unconfined aquifer model in the saturated zone.
96 Examples of one-dimensional Type-2 models include Liang et al. (2003), Yeh and
97 Eltahir (2005), Niu et al. (2007), and Zeng and Decker (2009). Examples of quasi
98 three-dimensional Type-2 models are York et al. (2002); Fan et al. (2007); Miguez-
99 Macho et al. (2007); and Shen et al. (2013). Type-3 models include a three-
100 dimensional representation of subsurface flow based on the variably saturated

101 Richards equation (Maxwell and Miller, 2005; Tian et al., 2012). Type-3 models
102 employ a unified treatment of hydrologic processes in the vadose and phreatic zones
103 but lump changes associated with water density and unconfined aquifer porosity into
104 a specific storage term. The fourth class (Type-4) of subsurface flow and reactive
105 transport models (e.g., PFLOTRAN (Hammond and Lichtner, 2010), TOUGH2 (Pruess
106 et al., 1999), and STOMP (White and STOMP, 2000)) combine a water equation of
107 state (EoS) and soil compressibility with the variably saturated Richards equation.
108 Type-4 models have not been routinely coupled with LSMs to address climate change
109 relevant research questions. Clark et al. (2015) summarized that most LSMs use
110 different physics formulations for representing hydrologic processes in saturated and
111 unsaturated zones. Additionally, Clark et al. (2015) identified incorporation of
112 variably saturated hydrologic flow models (i.e., Type-3 and Type-4 models) in LSMs
113 as a key opportunity for future model development that is expected to improve
114 simulation of coupled soil moisture and shallow groundwater dynamics.

115 The Energy, Exascale, Earth System Model (E3SM) is a new Earth System
116 Modeling project sponsored by the U.S. Department of Energy (DOE) (E3SM Project,
117 2018). The E3SM model started from the Community Earth System Model (CESM)
118 version 1_3_beta10 (Oleson, 2013). Specifically, the initial version (v0) of the E3SM
119 Land Model (ELM) was based off the Community Land Model's (CLM's) tag 4_5_71.
120 ELMv0 uses a Type-2 subsurface hydrology model based on Zeng and Decker (2009).
121 In this work, we developed in ELMv1 a Type-4 Variably Saturated Flow model (VSFM)
122 to provide a unified treatment of soil hydrologic processes within the unsaturated
123 and saturated zones. The VSFM formulation is based on the isothermal, single phase,
124 variably-saturated (RICHARDS) flow model within PFLOTRAN (Hammond and
125 Lichtner, 2010). While PFLOTRAN is a massively parallel, three-dimensional
126 subsurface model, the VSFM is a serial, one-dimensional model that is appropriate for
127 climate scale applications.

128 This paper is organized into several sections: (1) brief review of the ELMv0
129 subsurface hydrology model; (2) overview of the VSFM formulation integrated in
130 ELMv1; (3) application of the new model formulation to three benchmark problems;
131 (4) development of a subsurface drainage parameterization necessary to predict

132 global water table depths (WTDs) comparable to recently released observationally-
 133 constrained estimates; (5) comparison of ELMv1 global simulations with the default
 134 subsurface hydrology model and VSFM against multiple observations using the
 135 International Land Model Benchmarking package (ILAMB; Hoffman et al. (2017));
 136 and (6) a summary of major findings.

137 **2 Methods**

138 **2.1 Current Model Formulation**

139 Water flow in the unsaturated zone is often described by the θ -based Richards
 140 equation:

$$\frac{\partial \theta}{\partial t} = -\nabla \cdot \mathbf{q} - Q \quad (1)$$

141

142 where θ [m^3 of water m^{-3} of soil] is the volumetric soil water content, t [s] is time, \mathbf{q}
 143 [m s^{-1}] is the Darcy water flux, and Q [m^3 of water m^{-3} of soil s^{-1}] is a soil moisture
 144 sink term. The Darcy flux, \vec{q} , is given by

$$\mathbf{q} = -K\nabla(\psi + z) \quad (2)$$

145 where K [ms^{-1}] is the hydraulic conductivity, z [m] is height above some datum in the
 146 soil column and ψ [m] is the soil matric potential. The hydraulic conductivity and soil
 147 matric potential are modeled as non-linear function of volumetric soil moisture
 148 following Clapp and Hornberger (1978):

$$K = \Theta_{ice} K_{sat} \left(\frac{\theta}{\theta_{sat}} \right)^{2B+3} \quad (3)$$

$$\psi = \psi_{sat} \left(\frac{\theta}{\theta_{sat}} \right)^{-B} \quad (4)$$

149

150 where K_{sat} [m s^{-1}] is saturated hydraulic conductivity, ψ_{sat} [m] is saturated soil
 151 matric potential, B is a linear function of percentage clay and organic content (Oleson,
 152 2013), and Θ_{ice} is the ice impedance factor (Swenson et al., 2012). ELMv0 uses the

153 modified form of Richards equation of Zeng and Decker (2009) that computes Darcy
154 flux as

$$\mathbf{q} = -K\nabla(\psi + z - C) \quad (5)$$

155 where C is a constant hydraulic potential above the water table, z_{∇} , given as

$$C = \psi_E + z = \psi_{sat} \left(\frac{\theta_E(z)}{\theta_{sat}} \right)^{-B} + z = \psi_{sat} + z_{\nabla} \quad (6)$$

156 where ψ_E [m] is the equilibrium soil matric potential, z [m] is height above a
157 reference datum, θ_E [m³ m⁻³] is volumetric soil water content at equilibrium soil
158 matric potential, and z_{∇} [m] is height of water table above a reference datum. ELMv0
159 uses a cell-centered finite volume spatial discretization and backward Euler implicit
160 time integration. By default, ELMv0's vertical discretization of a soil column yields 15
161 soil layers of exponentially varying soil thicknesses that reach a depth of 42.1 m Only
162 the first 10 soils layers (or top 3.8 m of each soil column), are hydrologically active,
163 while thermal processes are resolved for all 15 soils layers. The nonlinear Darcy flux
164 is linearized using Taylor series expansion and the resulting tridiagonal system of
165 equations is solved by LU factorization.

166 Flow in the saturated zone is modeled as an unconfined aquifer below the soil
167 column based on the work of Niu et al. (2007). Exchange of water between the soil
168 column and unconfined aquifer depends on the location of the water table. When the
169 water table is below the last hydrologically active soil layer in the column, a recharge
170 flux from the last soil layer replenishes the unconfined aquifer. A zero-flux boundary
171 condition is applied to the last hydrologically active soil layer when the water table is
172 within the soil column. The unconfined aquifer is drained by a flux computed based
173 on the SIMTOP scheme of Niu et al. (2007) with modifications to account for frozen
174 soils (Oleson, 2013).

175 **2.2 New VSFM Model Formulation**

176 In the VSFM formulation integrated in ELMv1, we use the mass conservative form of
177 the variably saturated subsurface flow equation (Farthing et al., 2003; Hammond and
178 Lichtner, 2010; Kees and Miller, 2002):

$$\frac{\partial(\phi s_w \rho)}{\partial t} = -\nabla \cdot (\rho \mathbf{q}) - Q \quad (7)$$

179 where ϕ [m³ m⁻³] is the soil porosity, s_w [-] is saturation, ρ [kg m⁻³] is water density,
 180 \mathbf{q} [m s⁻¹] is the Darcy velocity, and Q [kg m⁻³ s⁻¹] is a water sink. We restrict our model
 181 formulation to a one-dimensional system and the flow velocity is defined by Darcy's
 182 law:

$$\mathbf{q} = -\frac{k k_r}{\mu} \nabla (P + \rho g z) \quad (8)$$

183 where k [m²] is intrinsic permeability, k_r [-] is relative permeability, μ [Pa s] is
 184 viscosity of water, P [Pa] is pressure, g [m s⁻²] is the acceleration due to gravity, and
 185 z [m] is elevation above some datum in the soil column.

186 In order to close the system, a constitutive relationship is used to express
 187 saturation and relative permeability as a function of soil matric pressure. Analytic
 188 Water Retention Curves (WRCs) are used to model effective saturation (s_e)

$$s_e = \left(\frac{s_w - s_r}{1 - s_r} \right) \quad (9)$$

189 where s_w is saturation and s_r is residual saturation. We have implemented Brooks
 190 and Corey (1964) (equation 10) and van Genuchten (1980) (equation 11) WRCs:

$$s_e = \begin{cases} \left(\frac{-P_c}{P_c^0} \right)^{-\lambda} & \text{if } P_c < 0 \\ 1 & \text{if } P_c \geq 0 \end{cases} \quad (10)$$

$$s_e = \begin{cases} [1 + (\alpha |P_c|)^n]^{-m} & \text{if } P_c < 0 \\ 1 & \text{if } P_c \geq 0 \end{cases} \quad (11)$$

191 where P_c [Pa] is the capillary pressure, P_c^0 [Pa] is the air entry pressure, and α [Pa⁻¹]
 192 is inverse of the air entry pressure . The capillary pressure is computed as $P_c = P -$
 193 P_{ref} where P_{ref} is P_c^0 for Brooks and Corey WRC and typically the atmospheric
 194 pressure (=101,325 [Pa]) is used for van Genuchten WRC. In addition, a smooth
 195 approximation of equation (10) and (11) was developed to facilitate convergence of
 196 the nonlinear solver (Appendix A). Relative soil permeability was modeled using the
 197 Mualem (1976) formulation:

$$\kappa_r(s_e) = \begin{cases} s_e^{0.5} \left[1 - \left(1 - s_e^{1/m} \right)^m \right] & \text{if } P < P_{ref} \\ 1 & \text{if } P \geq P_{ref} \end{cases} \quad (12)$$

198 Lastly, we used an EoS for water density, ρ , that is a nonlinear function of liquid
199 pressure, P , and liquid temperature, T , given by Tanaka et al. (2001):

$$\rho(P, T) = \left[1 + (k_0 + k_1 T + k_2 T^2)(P - P_{ref}) \right] a_5 \left[1 - \frac{(T + a_1)^2 (T + a_2)}{a_3 (T + a_4)} \right] \quad (13)$$

200 where

$$k_0 = 50.74 \times 10^{-11} \text{ [Pa}^{-1}\text{]}$$

$$k_1 = -0.326 \times 10^{-11} \text{ [Pa}^{-1}\text{C}^{-1}\text{]}$$

$$k_2 = 0.00416 \times 10^{-11} \text{ [Pa}^{-1}\text{C}^2\text{]}$$

$$a_1 = -3.983035 \text{ [C]}$$

$$a_2 = 301.797 \text{ [C]}$$

$$a_3 = 522558.9 \text{ [C}^{-2}\text{]}$$

$$a_4 = 69.34881 \text{ [C]}$$

$$a_5 = 999.974950 \text{ [kg m}^{-3}\text{]}$$

201 Unlike the default subsurface hydrology model, the VSFM is applied over the
202 full sol depth (in the default model, 15 soils layers). The VSFM model replaces both
203 the θ -based Richards equation and the unconfined aquifer of the default model and
204 uses a zero-flux lower boundary condition. In the VSFM model, water table depth is
205 diagnosed based on the vertical soil liquid pressure profile. Like the default model,
206 drainage flux is computed based on the modified SIMTOP approach and is vertically
207 distributed over the soil layers below the water table.

208 2.2.1 Discrete Equations

209 We use a cell-centered finite volume discretization to decompose the spatial
210 domain, Ω , into N non-overlapping control volumes, Ω_n , such that $\Omega = \cup_{n=1}^N \Omega_n$ and Γ_n
211 represents the boundary of the n -th control volume. Applying a finite volume integral
212 to equation (7) and the divergence theorem yields

$$\frac{\partial}{\partial t} \int_{\Omega_n} (\phi s_w \rho) dV = - \int_{\Gamma_n} (\rho \mathbf{q}) \cdot d\mathbf{A} - \int_{\Omega_n} Q dV \quad (14)$$

213 The discretized form of the left hand side term and first term on the right hand side
 214 of equation (14) are approximated as:
 215

$$\frac{\partial}{\partial t} \int_{\Omega_n} (\phi s_w \rho) dV \approx \left(\frac{d}{dt} (\phi s_w \rho) \right) V_n \quad (15)$$

$$\int_{\Gamma_n} (\rho \mathbf{q}) \cdot d\mathbf{A} \approx \sum_{n'} (\rho \mathbf{q})_{nn'} \cdot \mathbf{A}_{nn'} \quad (16)$$

216 After substituting equations (15) and (16) in equation (14), the resulting ordinary
 217 differential equation for the variably saturated flow model is

$$\left(\frac{d}{dt} (\phi s_w \rho) \right) V_n = - \sum_{n'} (\rho \mathbf{q})_{nn'} \cdot \mathbf{A}_{nn'} - Q_n V_n \quad (17)$$

218 We perform temporal integration of equation (17) using the backward-Euler scheme:

$$\left(\frac{(\phi s_w \rho)_n^{t+1} - (\phi s_w \rho)_n^t}{\Delta t} \right) V_n = - \sum_{n'} (\rho \mathbf{q})_{nn'}^{t+1} \cdot \mathbf{A}_{nn'} - Q_n^{t+1} V_n \quad (18)$$

219 Rearranging terms of equation (18) results in a nonlinear equation for the unknown
 220 pressure at timestep $t + 1$ as

$$\left(\frac{(\phi s_w \rho)_n^{t+1} - (\phi s_w \rho)_n^t}{\Delta t} \right) V_n + \sum_{n'} (\rho \mathbf{q})_{nn'}^{t+1} \cdot \mathbf{A}_{nn'} + Q_n^{t+1} V_n = 0 \quad (19)$$

221 In this work, we find the solution to the nonlinear system of nonlinear equations given
 222 by equation (19) using Newton's method via the Scalable Nonlinear Equations Solver
 223 (SNES) within the Portable, Extensible Toolkit for Scientific Computing (PETSc)
 224 library (Balay et al., 2016). PETSc provides a suite of data structures and routines for
 225 the scalable solution of partial differential equations. VSFM uses the composable data
 226 management (DMComposite) provided by PETSc (Brown et al., 2012), which enables
 227 the potential future application of the model to solve tightly coupled multi-
 228 component, multi-physics processes as discussed in section 3.4. A Smooth
 229 approximation of the Brooks and Corey (1964) (SBC) water retention curve was
 230 developed to facilitate faster convergence of the nonlinear solver (Appendix A).
 231 ELMv0 code for subsurface hydrologic processes only supports two vertical mesh

232 configurations and a single set of boundary and source-sink conditions. Moreover, the
233 monolithic ELMv0 code does not allow for testing of individual process
234 representations against analytical solutions or simulation results from other models.
235 The modular software design of VSFM overcomes ELMv0's software limitation by
236 allowing VSFM code to be built independently of the ELM code. This flexibility of
237 VSFM's build system allows for testing of the VSFM physics in isolation without any
238 influence from the rest of ELM's physics formulations. Additionally, VSFM can be
239 easily configured for a wide range of benchmark problems with different spatial grid
240 resolutions, material properties, boundary conditions, and source-sink forcings.

241 **2.3 VSFM single-column evaluation**

242 We tested the VSFM with three idealized 1-dimensional test problems. First, the
243 widely studied problem for 1D Richards equation of infiltration in dry soil by Celia et
244 al. (1990) was used. The problem setup consists of a 1.0 m long soil column with a
245 uniform initial pressure of -10.0 m (= 3535.5 Pa). Time invariant boundary
246 conditions applied at the top and bottom of soil column are -0.75 m (= 93989.1 Pa)
247 and -10.0 m (= 3535.5 Pa), respectively. The soil properties for this test are given in
248 Table 1. A vertical discretization of 0.01 m is used in this simulation.

249 Second, we simulated transient one-dimensional vertical infiltration in a two-
250 layered soil system as described in Srivastava and Yeh (1991). The domain consisted
251 of a 2 m tall soil column divided equally in two soil types. Except for soil intrinsic
252 permeability, all other soil properties of the two soil types are the same. The bottom
253 soil is 10 times less permeable than the top (Table1). Unlike Srivastava and Yeh
254 (1991), who used exponential functions of soil liquid pressure to compute hydraulic
255 conductivity and soil saturation, we used Mualem (1976) and van Genuchten (1980)
256 constitutive relationships. Since our choice of constitutive relationships for this setup
257 resulted in absence of an analytical solution, we compared VSFM simulations against
258 PFLOTRAN results. The domain was discretized in 200 control volumes of equal soil
259 thickness. Two scenarios, wetting and drying, were modeled to test the robustness of
260 the VSFM solver robustness. Initial conditions for each scenario included a time
261 invariant boundary condition of 0 m (= 1.01325×10^5 Pa) for the lowest control

262 volume and a constant flux of 0.9 cm hr⁻¹ and 0.1 cm hr⁻¹ at the soil surface for wetting
263 and drying scenarios, respectively.

264 Third, we compare VSFM and PFLOTRAN predictions for soil under variably
265 saturated conditions. The 1-dimensional 1 m deep soil column was discretized in 100
266 equal thickness control volumes. A hydrostatic initial condition was applied such that
267 water table is 0.5 m below the soil surface. A time invariant flux of 2.5×10^{-5} m s⁻¹ is
268 applied at the surface, while the lowest control volume has a boundary condition
269 corresponding to the initial pressure value at the lowest soil layer. The soil properties
270 used in this test are the same as those used in the first evaluation.

271 **2.4 Global Simulations and groundwater depth analysis**

272 We performed global simulations with ELMv1-VSFM at a spatial resolution of
273 1.9° (latitude) \times 2.5° (longitude) with a 30 [min] time-step for 200 years, including a
274 180 year spinup and the last 20 years for analysis. The simulations were driven by
275 CRUNCEP meteorological forcing from 1991-2010 (Piao et al., 2012) and configured
276 to use prescribed satellite phenology.

277 For evaluation and calibration, we used the Fan et al. (2013) global \sim 1 km
278 horizontal resolution WTD dataset (hereafter F2013 dataset), which is based on a
279 combination of observations and hydrologic modeling. We aggregated the dataset to
280 the ELMv1-VSFM spatial resolution. ELM-VSFM's default vertical soil discretization
281 uses 15 soil layers to a depth of \sim 42 m, with an exponentially varying soil thickness.
282 However, \sim 13% of F2013 land gridcells have a water table deeper than 42 m. We
283 therefore modified ELMv1-VSFM to extend the soil column to a depth of 150 m with
284 59 soil layers; the first nine soil layer thicknesses were the same as described in
285 Oleson (2013) and the remaining layers (10-59) were set to a thickness of 3 m.

286 **2.5 Estimation of the subsurface drainage parameterization**

287 In the VSFM formulation, the dominant control on long-term GW depth is the
288 subsurface drainage flux, q_d [kg m⁻² s⁻¹], which is calculated based on water table
289 depth, z_v [m], (Niu et al. (2005)):

$$q_d = q_{d,max} \exp(-f_d z_v) \quad (20)$$

290 where $q_{d,max}$ [$\text{kg m}^{-2} \text{s}^{-1}$] is the maximum drainage flux that depends on gridcell slope
291 and f_d [m^{-1}] is an empirically-derived parameter. The subsurface drainage flux
292 formulation of Niu et al. (2005) is similar to the TOPMODEL formulation (Beven and
293 Kirkby, 1979) and assumes the water table is parallel to the soil surface. While
294 Sivapalan et al. (1987) derived $q_{d,max}$ as a function of lateral hydraulic anisotropy,
295 hydraulic conductivity, topographic index, and decay factor controlling vertical
296 saturated hydraulic conductivity, Niu et al. (2005) defined $q_{d,max}$ as a single
297 calibration parameter. ELMv0 uses $f_d = 2.5 \text{ m}^{-1}$ as a global constant and estimates
298 maximum drainage flux when WTD is at the surface as $q_{d,max} = 10 \sin(\beta) \text{ kg m}^{-2} \text{ s}^{-1}$.
299 1. Of the two parameters, f_d and $q_{d,max}$, available for model calibration, we choose to
300 calibrate f_d because the uncertainty analysis by Hou et al. (2012) identified it as the
301 most significant hydrologic parameter in CLM4. To improve on the f_d parameter
302 values, we performed an ensemble of global simulations with f_d values of 0.1, 0.2, 0.5,
303 1.0, 2.5, 5.0, 10.0, and 20 m^{-1} . Each ensemble simulation was run for 200 years to
304 ensure an equilibrium solution, and the last 20 years were used for analysis. A non-
305 linear functional relationship between f_d and WTD was developed for each gridcell
306 and then the F2013 dataset was used to estimate an optimal f_d for each gridcell.

307 **2.6 Global ELM-VSFM evaluation**

308 With the optimal f_d values, we ran a ELM-VSFM simulation using the protocol
309 described above. We then used the International Land Model Benchmarking package
310 (ILAMB) to evaluate the ELMv1-VSFM predictions of surface energy budget, total
311 water storage anomalies (TWSA), and river discharge (Collier et al., 2018; Hoffman et
312 al., 2017). ILAMB evaluates model prediction bias, RMSE, and seasonal and diurnal
313 phasing against multiple observations of energy, water, and carbon cycles at in-situ,
314 regional, and global scales. Since ELM-VSFM simulations in this study did not include
315 an active carbon cycle, we used the following ILAMB benchmarks for water and
316 energy cycles: (i) latent and surface energy fluxes using site-level measurements from
317 FLUXNET (Lasslop et al., 2010) and globally from FLUXNET-MTE (Jung et al., 2009));
318 (ii) terrestrial water storage anomaly (TWSA) from the Gravity Recovery And Climate
319 Experiment (GRACE) observations (Kim et al., 2009); and (iii) stream flow for the 50

320 largest global river basins (Dai and Trenberth, 2002). We applied ILAMB benchmarks
321 for ELMv1-VSFM simulations with default and calibrated f_d to ensure improvements
322 in WTD predictions did not degrade model skill for other processes.

323 **3 Results and discussion**

324 **3.1 VSFM single-column evaluation**

325 For the 1D Richards equation infiltration in dry soil comparison, we evaluated
326 the solutions at 24-hr against those published by Celia et al. (1990) (Figure 1). The
327 VSFM solver accurately represented the sharp wetting front over time, where soil
328 hydraulic properties change dramatically due to non-linearity in the soil water
329 retention curve.

330 For the model evaluation of infiltration and drying in layered soil, the results of
331 the VSFM and PFLOTRAN are essentially identical. In both models and scenarios, the
332 higher permeability top soil responds rapidly to changes in the top boundary
333 condition and the wetting and drying fronts progressively travel through the less
334 permeable soil layer until soil liquid pressure in the entire column reaches a new
335 steady state by about 100 h (Figure 2).

336 We also evaluated the VSFM predicted water table dynamics against PFLOTRAN
337 predictions from an initial condition of saturated soil below 0.5 m depth. The
338 simulated water table rises to 0.3 m depth by 1 day and reaches the surface by 2 days,
339 and the VSFM and PFLOTRAN predictions are essentially identical Figure 3. These
340 three evaluation simulations demonstrate the VSFM accurately represents soil
341 moisture dynamics under conditions relevant to ESM-scale prediction.

342 **3.2 Subsurface drainage parameterization estimation**

343 The simulated nonlinear WTD- f_d relationship is a result of the subsurface
344 drainage parameterization flux given by equation (20) (Figure 4(a) and (b)). For
345 $0.1 \leq f_d \leq 1$, the slope of the WTD- f_d relationship for all gridcells is log-log linear
346 with a slope of -1.0 ± 0.1 . The log-log linear relationship breaks down for $f_d > 1$,
347 where the drainage flux becomes much smaller than infiltration and

348 evapotranspiration (Figure 4(c) and (d)). Thus, at larger f_d , the steady state z_v
349 becomes independent of f_d and is determined by the balance of infiltration and
350 evapotranspiration.

351 For 79% of the global gridcells, the ensemble range of simulated WTD spanned
352 the F2013 dataset. The optimal value of f_d for each of these gridcells was obtained by
353 linear interpolation in the log-log space (e.g., Figure 4 (a)). For the remaining 21% of
354 gridcells where the shallowest simulated WTD across the range of f_d was deeper than
355 that in the F2013 dataset, the optimal f_d value was chosen as the one that resulted in
356 the lowest absolute WTD error (e.g., Figure 4 (b)). At large f_d values, the drainage flux
357 has negligible effects on WTD, yet simulated WTD is not sufficiently shallow to match
358 the F2013 observations, which indicates that either evapotranspiration is too large
359 or infiltration is too small. There was no difference in the mean percentage of sand
360 and clay content between grids cells with and without an optimal f_d value. The
361 optimal f_d has a global average of $1.60 \text{ m}^{-1} \pm 2.68 \text{ m}^{-1}$ and 72% of global gridcells have
362 an optimal f_d value lower than the global average (Figure 5).

363 **3.3 Global simulation evaluation**

364 The ELMv1-VSFM predictions are much closer to the F2013 dataset (Figure 6a)
365 using optimal globally-distributed f_d values (Figure 6c) compared to the default f_d
366 value (Figure 6b). The significant reduction in WTD bias (model – observation) is
367 mostly due to improvement in the model’s ability to accurately predict deep WTD
368 using optimal f_d values. In the simulation using optimal globally-distributed f_d
369 values, all gridcells with WTD bias > 3.7 m were those for which an optimal f_d was
370 not found. The mean global bias, RMSE, and R^2 values improved in the new ELMv1-
371 VSFM compared to the default model (Table 1). The 79% of global grid cells for which
372 an optimal f_d value was estimated had significantly better water table prediction
373 with a bias, RMSE, and R^2 of -0.04 m, 0.67 m, and 0.99, respectively, as compared to
374 the remaining 21% of global gridcells that had a bias, RMSE, and R^2 of -9.82 m, 18.08
375 m, and 0.31, respectively. The simulated annual WTD range, which we define to be
376 the difference between maximum and minimum WTD in a year, has a spatial mean
377 and standard deviation of 0.32 m and 0.58 m, respectively, using optimal f_d values

378 (Figure 7 (a)). The annual WTD range decreased by 0.24 m for the 79% of the grid
379 cells for which an optimal f_d value was estimated (Figure 7 (b)).

380 Globally-averaged WTD in ELMv1-VSFM simulations with default f_d and
381 optimal f_d values were 10.5 m and 20.1 m, respectively. Accurate prediction of deep
382 WTD in the simulation with optimal f_d caused very small differences in near-surface
383 soil moisture (Figure 8). The 79% of grid cells with an optimal f_d value had deeper
384 globally-averaged WTDs than when using the default f_d value (24.3 m vs. 8.6 m). For
385 these 79% of grid cells, the WTD was originally deep enough to not impact near-
386 surface conditions (Kollet and Maxwell, 2008); therefore, further lowering of WTD
387 led to negligible changes in near-surface hydrological conditions.

388 The International Land Model Benchmarking (ILAMB) package (Hoffman et al.,
389 2017) provides a comprehensive evaluation of predictions of carbon cycle states and
390 fluxes, hydrology, surface energy budgets, and functional relationships by
391 comparison to a wide range of observations. We used ILAMB to evaluate the
392 hydrologic and surface energy budget predictions from the new ELMv1-VSFM model
393 (Table 3). Optimal f_d values had inconsequential impacts on simulated surface
394 energy fluxes at site-level and global scales. Optimal f_d values led to improvement in
395 prediction of deep WTD (with a mean value of 24.3 m) for grid cells that had an
396 average WTD of 8.7 m in the simulation using default f_d values. Thus, negligible
397 differences in surface energy fluxes between the two simulations are consistent with
398 the findings of Kollet and Maxwell (2008), who identified decoupling of groundwater
399 dynamics and surface processes at a WTD of ~ 10 m. There were slight changes in bias
400 and RMSE for predicted TWSA, but the ILAMB score remained unchanged. The TWSA
401 amplitude is lower for the simulation with optimal f_d values, consistent with the
402 associated decrease in annual WTD range. ELM's skill in simulating runoff for the 50
403 largest global watersheds remained unchanged.

404 Finally, we evaluated the computational costs of implementing VSFM in ELM
405 and compared them to the default model. We performed 5-year long simulations for
406 default and VSFM using 96, 192, 384, 768, and 1536 cores on the Edison
407 supercomputer at the National Energy Research Scientific Computing Center. Using
408 an optimal processor layout, we found that ELMv1-VSFM is $\sim 30\%$ more expensive

409 than the default ELMv1 model. We note that the relative computational cost of the
410 land model in a fully coupled global model simulation is generally very low. Dennis et
411 al. (2012) reported computational cost of the land model to be less than 1% in ultra-
412 high-resolution CESM simulations. We therefore believe that the additional benefits
413 associated with the VSFM formulation are well justified by this modest increase in
414 computational cost. In particular, VSFM allows a greater variety of mesh
415 configurations and boundary conditions, and can accurately simulate WTD for the
416 ~13% of global grid cells that have a water table deeper than 42 [m] (Fan et al. (2013).

417 **3.4 Caveats and Future Work**

418 The significant improvement in WTD prediction using optimal f_d values
419 demonstrates VSFM's capabilities to model hydrologic processes using a unified
420 physics formulation for unsaturated-saturated zones. However, several caveats
421 remain due to uncertainties in model structure, model parameterizations, and climate
422 forcing data.

423 In this study, we assumed a spatially homogeneous depth to bedrock (DTB) of
424 150 m. Recently, Brunke et al. (2016) incorporated a global ~1 km dataset of soil
425 thickness and sedimentary deposits (Pelletier et al., 2016) in CLM4.5 to study the
426 impacts of soil thickness spatial heterogeneity on simulated hydrological and thermal
427 processes. While inclusion of heterogeneous DTB in CLM4.5 added more realism to
428 the simulation setup, no significant changes in simulated hydrologic and energy
429 fluxes were reported by Brunke et al. (2016). Presently, work is ongoing in the E3SM
430 project to include variable DTB within ELM and future simulations will examine the
431 impact of those changes on VSFM's prediction of WTD. Our use of the 'satellite
432 phenology' mode, which prescribes transient LAI profiles for each plant functional
433 type in the gridcell, ignored the likely influence of water cycle dynamics and nutrient
434 constraints on the C cycle (Ghimire et al., 2016; Zhu et al., 2016). Estimation of soil
435 hydraulic properties based on soil texture data is critical for accurate LSM predictions
436 (Gutmann and Small, 2005) and this study does not account for uncertainty in soil
437 hydraulic properties.

438 Lateral water redistribution impacts soil moisture dynamics (Bernhardt et al.,
439 2012), biogeochemical processes in the root zone (Grant et al., 2015), distribution of
440 vegetation structure (Hwang et al., 2012), and land-atmosphere interactions (Chen
441 and Kumar, 2001; Rihani et al., 2010). The ELMv1-VSFM developed in this study does
442 not include lateral water redistribution between soil columns and only simulates
443 vertical water transport. Lateral subsurface processes can be included in LSMs via a
444 range of numerical discretization approaches of varying complexity, e.g., adding
445 lateral water as source/sink terms in the 1D model, implementing an operator split
446 approach to solve vertical and lateral processes in a non-iterative approach (Ji et al.,
447 2017), or solving a fully coupled 3D model (Bisht et al., 2017; Bisht et al., 2018; Kollet
448 and Maxwell, 2008). Additionally, lateral transport of water can be implemented in
449 LSMs at a subgrid level (Milly et al., 2014) or grid cell level (Miguez-Macho et al.,
450 2007). The current implementation of VSFM is such that each processor solves the
451 variably saturated Richards equation for all independent soil columns as one single
452 problem. Thus, extension of VSFM to solve the tightly coupled 3D Richards equation
453 on each processor locally while accounting for lateral transport of water within grid
454 cells and among grid cells is straightforward. The current VSFM implementation can
455 also be easily extended to account for subsurface transport of water among grid cells
456 that are distributed across multiple processors by modeling lateral flow as
457 source/sink terms in the 1D model. Tradeoffs between approaches to represent
458 lateral processes and computational costs need to be carefully studied before
459 developing quasi or fully three-dimensional land surface models (Clark et al., 2015).

460 Transport of water across multiple components of the Soil Plant Atmosphere
461 Continuum (SPAC) has been identified as a critical process in understanding the
462 impact of climate warming on the global carbon cycle (McDowell and Allen, 2015).
463 Several SPAC models have been developed by the ecohydrology community and
464 applied to study site-level processes (Amenu and Kumar, 2008; Bohrer et al., 2005;
465 Manoli et al., 2014; Sperry et al., 1998), yet implementation of SPAC models in global
466 LSMs is limited (Clark et al., 2015). Similarly, current generation LSMs routinely
467 ignore advective heat transport within the subsurface, which has been shown to be
468 important in high-latitude environments by multiple field and modeling studies

469 (Bense et al., 2012; Frampton et al., 2011; Grant et al., 2017; Kane et al., 2001). The
470 use of PETSc's DMComposite in VSFM provides flexibility for solving a tightly coupled
471 multi-component problem (e.g., transport of water through the soil-plant continuum)
472 and multi-physics problem (e.g., fully coupled conservation of mass and energy
473 equations in the subsurface). DMComposite allows for an easy assembly of a tightly
474 coupled multi-physics problem from individual physics formulations (Brown et al.,
475 2012).

476 **4 Summary and Conclusion**

477 Starting from the climate-scale land model ELMv0, we incorporated a unified
478 physics formulation to represent soil moisture and groundwater dynamics that are
479 solved using PETSc. Application of VSFM to three benchmarks problems
480 demonstrated its robustness to simulated subsurface hydrologic processes in
481 coupled unsaturated and saturated zones. Ensemble global simulations at $1.9^0 \times 2.5^0$
482 were performed for 200 years to obtain spatially heterogeneous estimates of the
483 subsurface drainage parameter, f_d , that minimized mismatches between predicted
484 and observed WTDs. In order to simulate the deepest water table reported in the Fan
485 et al. (2013) dataset, we used 59 vertical soil layers that reached a depth of 150 m.

486 An optimal f_d was obtained for 79% of the grids cells in the domain. For the
487 remaining 21% of grid cells, simulated WTD always remained deeper than observed.
488 Calibration of f_d significantly improved global WTD prediction by reducing bias and
489 RMSE and increasing R^2 . Grids without an optimal f_d were the largest contributor of
490 error in WTD predication. ILAMB benchmarks on simulations with default and
491 optimal f_d showed negligible changes to surface energy fluxes, TWSA, and runoff.
492 ILAMB metrics ensured that model skill was not adversely impacted for all other
493 processes when optimal f_d values were used to improve WTD prediction.

494

495 **5 Appendix**

496 **5.1 Smooth approximation of Brooks-Corey water retention curve**

497 The Brooks and Corey (1964) water retention curve of equation (10) has a
 498 discontinuous derivative at $P = P_c^0$. Figure A 1 illustrates an example. To improve
 499 convergence of the nonlinear solver at small capillary pressures, the smoothed
 500 Brooks-Corey function introduces a cubic polynomial, $B(P_c)$, in the neighborhood of
 501 P_c^0 .

$$s_e = \begin{cases} (-\alpha P_c)^{-\lambda} & \text{if } P_c \leq P_u \\ B(P_c) & \text{if } P_u < P_c < P_s \\ 1 & \text{if } P_s \leq P_c \end{cases} \quad (21)$$

502 where the breakpoints P_u and P_s satisfy $P_u < P_c^0 < P_s \leq 0$. The smoothing
 503 polynomial

$$B(P_c) = b_0 + b_1(P_c - P_s) + b_2(P_c - P_s)^2 + b_3(P_c - P_s)^3 \quad (22)$$

504 introduces four more parameters, whose values follow from continuity. In particular
 505 matching the saturated region requires $B(P_s) = b_0 = 1$, and a continuous derivative
 506 at $P_c = P_s$ requires $B'(P_s) = b_1 = 0$. Similarly, matching the value and derivative at
 507 $P_c = P_u$ requires

$$b_2 = \frac{-1}{\Delta^2} \left[3 - (\alpha P_u)^{-\lambda} \left(3 + \frac{\lambda \Delta}{P_u} \right) \right] \quad (23)$$

$$b_3 = \frac{-1}{\Delta^3} \left[2 - (\alpha P_u)^{-\lambda} \left(2 + \frac{\lambda \Delta}{P_u} \right) \right] \quad (24)$$

508 where $\Delta = P_u - P_s$. Note $P_u \leq \Delta < 0$.

509 In practice, setting P_u too close to P_c^0 can produce an unwanted local maximum
 510 in the cubic smoothing regime, resulting in $s_e > 1$. Avoiding this condition requires
 511 that $B(P_c)$ increase monotonically from $P_c = P_u$, where $B'(P_c) > 0$, to $P_c = P_s$, where
 512 $B'(P_c) = 0$. Thus a satisfactory pair of breakpoints ensures

$$B'(P_c) = [P_c - P_s][2b_2 + 3b_3(P_c - P_s)] > 0 \quad (25)$$

513 throughout $P_u \leq P_c < P_s$.

514 Let P_c^* denote a local extremum of B , so that $B'(P_c^*) = 0$. If $P_c^* \neq P_s$, it follows
 515 $P_c^* - P_s = -2b_2/(3b_3)$. Rewriting equation 22, $B'(P_c) = (P_c - P_s)3b_3(P_c - P_c^*)$ shows
 516 that $B'(P_c^*) > 0$ requires either: (1) $b_3 < 0$ and $P_c^* < P_u$; or (2) $b_3 > 0$ and $P_c^* > P_u$;

517 The first possibility places P_c^* outside the cubic smoothing regime, and so does not
 518 constrain the choice of P_u or P_s . The second possibility allows an unwanted local
 519 extremum at $P_u < P_c^* < P_s$. In this case, $b_3 > 0$ implies $b_2 < 0$ (since $P_c^* < P_s \leq 0$).
 520 Then since $B''(P_c^*) = -2b_2$, the local extremum is a maximum, resulting in $s_e(P_c^*) >$
 521 1.

522 Given a breakpoint P_s , one strategy for choosing P_u is to guess a value, then
 523 check whether the resulting b_2 and b_3 produces $P_u < P_c^* < P_s$. If so, P_u should be
 524 made more negative. An alternative strategy is to choose P_u in order to guarantee
 525 acceptable values for b_2 and b_3 . One convenient choice forces $b_2 = 0$. Another picks
 526 P_u in order to force $b_3 = 0$. Both of these reductions: (1) ensure $B(P_c)$ has a positive
 527 slope throughout the smoothing interval; (2) slightly reduce the computation cost of
 528 finding $s_e(P_c)$ for P_c on the smoothing interval; and (3) significantly reduce the
 529 computational cost of inverting the model, in order to find P_c as a function of s_e .

530 As shown in Figure A 1, the two reductions differ mainly in that setting $b_2 = 0$
 531 seems to produce narrower smoothing regions (probably due to the fact that this
 532 choice gives zero curvature at $P_c = P_s$, while $b_3 = 0$ yields a negative second
 533 derivative there). However, we have not verified this observation analytically.

534 Both reductions require solving a nonlinear expression either equation (23) or
 535 (24), for P_u . While details are beyond the scope of this paper, we note that we have
 536 used a bracketed Newton-Raphson's method. The search switches to bisection when
 537 Newton-Raphson would jump outside the bounds established by previous iterations,
 538 and by the requirement $P_u < P_c^0$. In any event, since the result of this calculation may
 539 be cached for use throughout the simulation, it need not be particularly efficient.

540 5.2 Residual equation of VSFM formulation

541 The residual equation for the VSFM formulation at $t + 1$ time level for n -th control
 542 volume is given by

$$R_n^{t+1} \equiv \left(\frac{(\phi s_w \rho)_n^{t+1} - (\phi s_w \rho)_n^t}{\Delta t} \right) V_n + \sum_{n'} (\rho \mathbf{q})_{nn'}^{t+1} \cdot \mathbf{A}_{nn'} + Q_n^{t+1} V_n = 0 \quad (26)$$

543 where ϕ [mm³ mm³] is the soil porosity, s_w [-] is saturation, ρ [kg m⁻³] is water
 544 density, $\vec{q}_{nn'}$ [m s⁻¹] is the Darcy flow velocity between n -th and n' -th control

545 volumes, $A_{nn'}$ [m s⁻¹] is the interface face area between n -th and n' -th control
 546 volumes Q [kg m⁻³ s⁻¹] is a sink of water. The Darcy velocity is computed as

$$\mathbf{q}_{nn'} = - \left(\frac{\kappa \kappa_r}{\mu} \right)_{nn'} \left[\frac{P_{n'} - P_n - \rho_{nn'} (\mathbf{g} \cdot \mathbf{d}_{nn'})}{d_n + d_{n'}} \right] \mathbf{n}_{nn'} \quad (27)$$

547 where κ [m⁻²] is intrinsic permeability, κ_r [-] is relative permeability, μ [Pa s] is
 548 viscosity of water, P [Pa] is pressure, \mathbf{g} [m s⁻²] is the acceleration due to gravity,
 549 d_n [m] and $d_{n'}$ [m] is distance between centroid of n -th and n' -th control volume to
 550 the common interface between the two control volumes, $\mathbf{d}_{nn'}$ is a distance vector
 551 joining centroid of n -th and n' -th control volume, and $\mathbf{n}_{nn'}$ is a unit normal vector
 552 joining centroid of n -th and n' -th control volume.

553 The density at the interface of control volume, $\rho_{nn'}$, is computed as inverse
 554 distance weighted average by

$$\rho_{nn'} = \omega_{n'} \rho_n + \omega_n \rho_{n'} \quad (28)$$

555 where ω_n and $\omega_{n'}$ are given by

$$\omega_n = \frac{d_{n'}}{d_n + d_{n'}} = (1 - \omega_{n'}) \quad (29)$$

556 The first term on the RHS of equation 27 is computed as the product of distance
 557 weighted harmonic average of intrinsic permeability, $k_{nn'}$, and upwinding of
 558 k_r/μ ($= \lambda$) as

$$\left(\frac{\kappa \kappa_r}{\mu} \right)_{nn'} = k_{nn'} \left(\frac{\kappa_r}{\mu} \right)_{nn'} = \left[\frac{k_n k_{n'} (d_n + d_{n'})}{k_n d_{n'} + k_{n'} d_n} \right] \lambda_{nn'} \quad (30)$$

559 where

$$\lambda_{nn'} = \begin{cases} (k_r/\mu)_n & \text{if } \vec{q}_{nn'} > 0 \\ (k_r/\mu)_{n'} & \text{otherwise} \end{cases} \quad (31)$$

560 By substituting equation 28, 29 and 30 in equation 27, we obtain

$$\mathbf{q}_{nn'} = - \left[\frac{k_n k_{n'}}{k_n d_{n'} + k_{n'} d_n} \right] \lambda_{nn'} [P_{n'} - P_n - \rho_{nn'} (\mathbf{g} \cdot \mathbf{d}_{nn'})] \mathbf{n}_{nn'} \quad (32)$$

561

562 5.3 Jacobian equation of VSFM formulation

563 The discretized equations of VSFM leads to a system of nonlinear equations given by

564 $\mathbf{R}^{t+1}(\mathbf{P}^{t+1}) = \mathbf{0}$, which are solved using Newton's method using the Portable,

565 Extensible Toolkit for Scientific Computing (PETSc) library. The algorithm of
 566 Newton's method requires solution of the following linear problem

$$\mathbf{J}^{t+1,k}(\mathbf{P}^{t+1,k}) \Delta \mathbf{P}^{t+1,k} = -\mathbf{R}^{t+1,k}(\mathbf{P}^{t+1,k}) \quad (33)$$

567 where $\mathbf{J}^{t+1,k}(\mathbf{P}^{t+1,k})$ is the Jacobian matrix. In VSFM, the Jacobian matrix is
 568 computed analytically. The contribution to the diagonal and off-diagonal entry of the
 569 Jacobian matrix from n -th residual equations are given by

$$J_{nn} = \frac{\partial R_n}{\partial P_n} = \left(\frac{V_n}{\Delta t}\right) \frac{\partial(\rho\phi s_w)}{\partial P_n} + \sum_{n'} \frac{\partial(\rho\mathbf{q})_{nn'}}{\partial P_n} A_{nn'} + \frac{\partial Q_n^{t+1}}{\partial P_n} V_n \quad (34)$$

$$J_{nn'} = \frac{\partial R_n}{\partial P_{n'}} = \sum_{n'} \frac{\partial(\rho\mathbf{q})_{nn'}}{\partial P_{n'}} A_{nn'} + \frac{\partial Q_n^{t+1}}{\partial P_{n'}} V_n \quad (35)$$

570 The derivative of the accumulation term in J_{nn} is computed as

$$\frac{\partial(\rho\phi s_w)}{\partial P_n} = \phi s_w \frac{\partial \rho}{\partial P_n} + \rho s_w \frac{\partial \phi}{\partial P_n} + \rho \phi \frac{\partial s_w}{\partial P_n} \quad (36)$$

571 The derivative of flux between n -th and n' -th control volume with respect to
 572 pressure of each control volume is given as

$$\frac{\partial(\rho\mathbf{q})_{nn'}}{\partial P_n} = \rho_{nn'} \frac{\partial \mathbf{q}_{nn'}}{\partial P_n} + \mathbf{q}_{nn'} \omega_n \frac{\partial \rho_n}{\partial P_n} \quad (37)$$

573

$$\frac{\partial(\rho\mathbf{q})_{nn'}}{\partial P_{n'}} = \rho_{nn'} \frac{\partial \mathbf{q}_{nn'}}{\partial P_{n'}} + \mathbf{q}_{nn'} \omega_{n'} \frac{\partial \rho_{n'}}{\partial P_{n'}} \quad (38)$$

574 Lastly, the derivative of Darcy velocity between n -th and n' -th control volume with
 575 respect to pressure of each control volume is given as

$$\frac{\partial \mathbf{q}_{nn'}}{\partial P_n} = \left[\frac{k_n k_{n'}}{k_n d_{n'} + k_{n'} d_n} \right] \lambda_{nn'} \left[1 + \omega_n (\mathbf{g} \cdot \mathbf{d}_{nn'}) \frac{\partial \rho_n}{\partial P_n} \right] \mathbf{n}_{nn'} + \mathbf{q}_{nn'} \frac{\partial(\ln(\lambda_{nn'}))}{\partial P_n} \quad (39)$$

$$\begin{aligned} \frac{\partial \mathbf{q}_{nn'}}{\partial P_{n'}} &= \left[\frac{k_n k_{n'}}{k_n d_{n'} + k_{n'} d_n} \right] \lambda_{nn'} \left[-1 + \omega_n (\mathbf{g} \cdot \mathbf{d}_{nn'}) \frac{\partial \rho_{n'}}{\partial P_{n'}} \right] \mathbf{n}_{nn'} \quad (40) \\ &+ \mathbf{q}_{nn'} \frac{\partial(\ln(\lambda_{nn'}))}{\partial P_{n'}} \end{aligned}$$

576

577 **6 Code availability**

578 The standalone VSFM code is available at <https://github.com/MPP-LSM/MPP>. Notes
579 on how to run the VSFM for all benchmark problems and compare results against
580 PFLOTRAN at <https://bitbucket.org/gbisht/notes-for-gmd-2018-44>.

581 The research was performed using E3SM v1.0 and the code is available at
582 <https://github.com/E3SM-Project/E3SM>.

583 **7 Competing interests**

584 The authors declare that they have no conflict of interest.

585

586 **8 Acknowledgements**

587 This research was supported by the Director, Office of Science, Office of Biological
588 and Environmental Research of the US Department of Energy under contract no. DE-
589 AC02-05CH11231 as part of the Energy Exascale Earth System Model (E3SM)
590 programs.

591

592 **9 Tables**

593 **Table 1 Soil properties used in the three test problems described in section**
 594 **2.3.**

Problem number	ϕ [-]	λ [-]	α [Pa ⁻¹]	k [m ²]
1	0.368	0.5	3.4257x10 ⁻⁴	8.3913x10 ⁻¹²
2	0.4	0.5455	4x10 ⁻⁴	2.5281x10 ⁻¹² (top layer) 2.5281x10 ⁻¹³ (bottom layer)
3	0.368	0.5	3.4257x10 ⁻⁴	8.3913x10 ⁻¹²

595

596 **Table 2 Bias, root mean square error (RMSE), and correlation (R²) between**
 597 **simulated water table depth and Fan et al. (2013) data.**

	Bias [m]	RMSE [m]	R²
For all grids in ELM simulation with default f_{drain}	-10.3	21.3	0.28
For all grids in ELM simulation with optimal f_{drain}	2.10	8.33	0.91
For 79% grids with optimal f_{drain} in ELM simulation with optimal f_{drain}	-0.04	0.67	0.99
For 21% grids without optimal f_{drain} in ELM simulation with optimal f_{drain}	-9.82	18.08	0.31

598

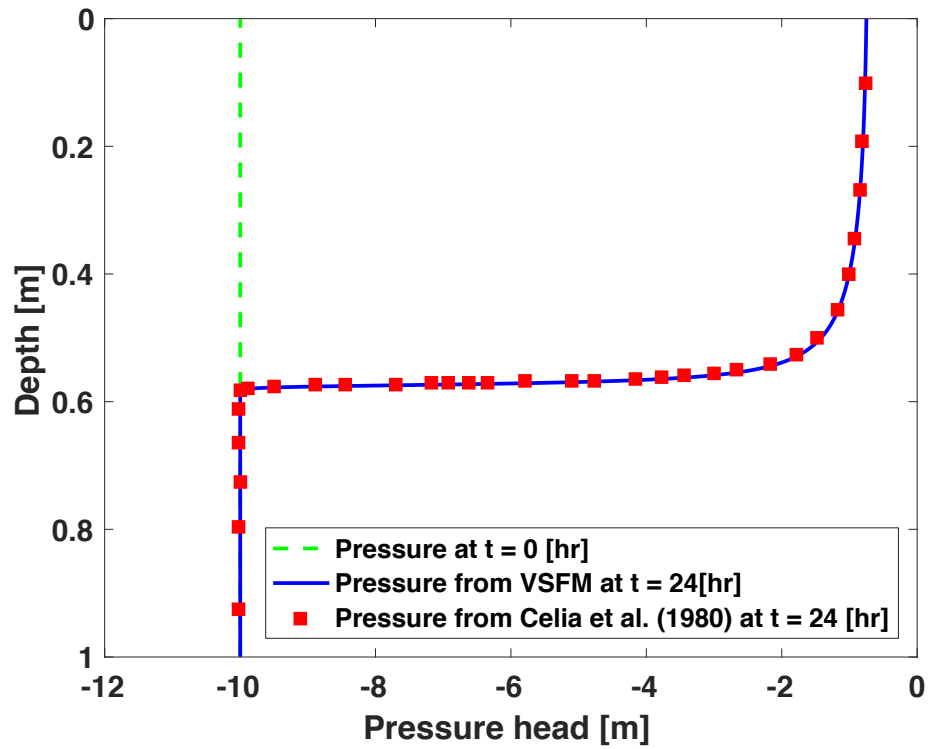
599

600 **Table 3 ILAMB benchmark scores for latent heat flux (LH), sensible heat flux**
601 **(SH), total water storage anomaly (TWSA), and surface runoff. The calculation**
602 **of ILAMB metrics and scores are described at <http://redwood.ess.uci.edu/>.**

	Data Source	Simulation with default f_d			Simulation with optimal f_d		
		Bias	RMSE	ILAMB Score	Bias	RMSE	ILAMB Score
LH	FLUXNET	10.1 [Wm ⁻²]	21.0 [Wm ⁻²]	0.68	9.5 [Wm ⁻²]	21.3 [Wm ⁻²]	0.68
	GBAF	7.1 [Wm ⁻²]	16.3 [Wm ⁻²]	0.81	6.3 [Wm ⁻²]	16.3 [Wm ⁻²]	0.81
SH	FLUXNET	6.7 [Wm ⁻²]	22.5 [Wm ⁻²]	0.66	7.1 [Wm ⁻²]	22.8 [Wm ⁻²]	0.65
	GBAF	6.9 [Wm ⁻²]	21.2 [Wm ⁻²]	0.71	7.6 [Wm ⁻²]	21.7 [Wm ⁻²]	0.70
TWSA	GRACE	1.3 [cm]	7.8 [cm]	0.48	3.0 [cm]	9.6 [cm]	0.48
Runoff	Dai	-0.26 [kg m ⁻² d ⁻¹]	0.91 [m ⁻² m ⁻² d ⁻¹]	0.52	-0.23 [kg m ⁻² d ⁻¹]	0.88 [kg m ⁻² d ⁻¹]	0.50

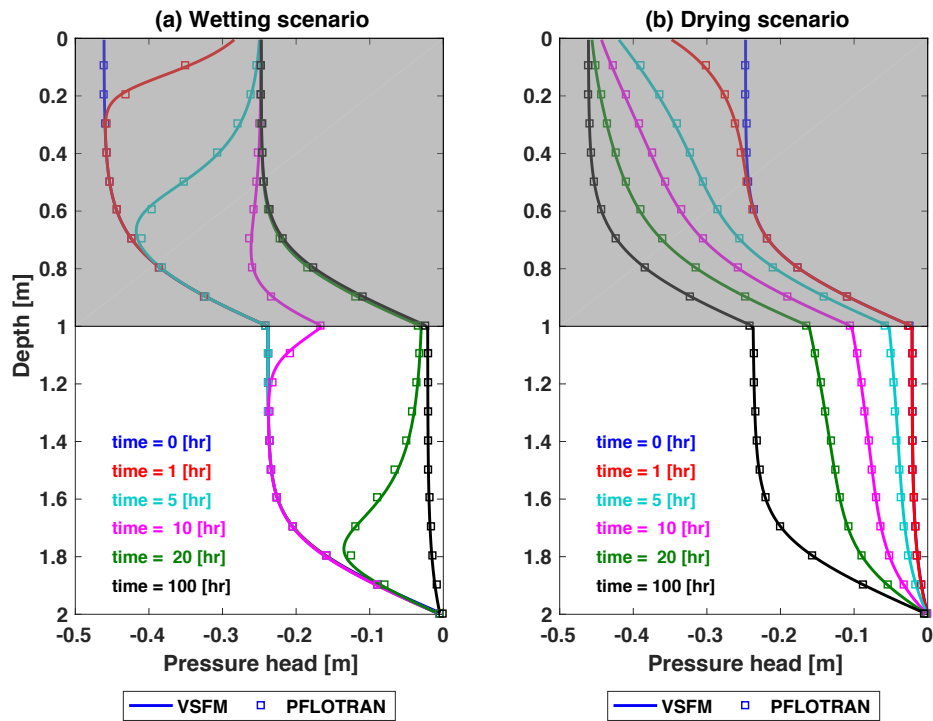
603

604



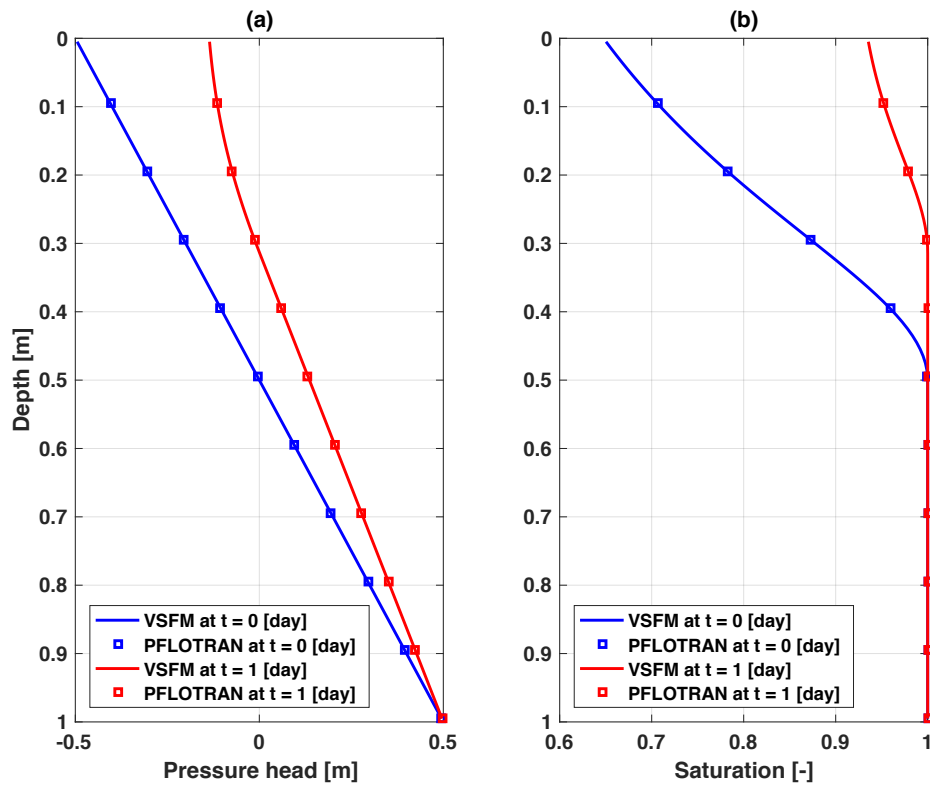
606

607 **Figure 1. Comparison of VFSM simulated pressure profile (blue line) against**
608 **data (red square) reported in Celia et al. (1990) at time = 24 hr for infiltration**
609 **in a dry soil column. Initial pressure condition is shown by green line.**



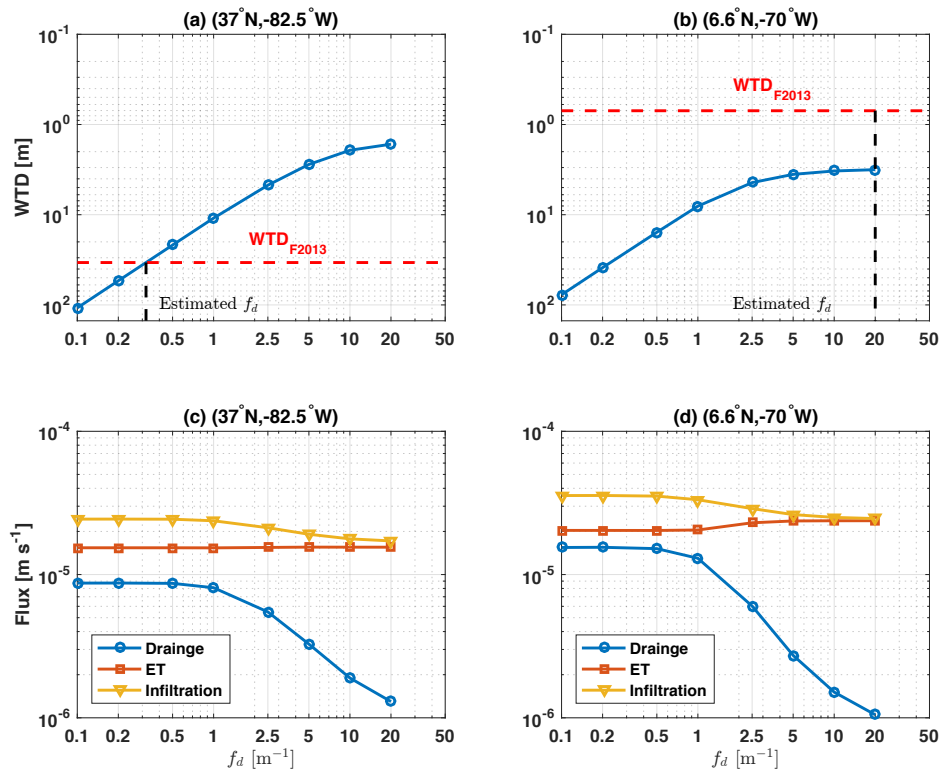
610

611 **Figure 2. Transient liquid pressure simulated for a two layer soil system by**
 612 **VSFM (solid line) and PFLOTRAN (square) for wetting (left) and drying (right)**
 613 **scenarios.**



614

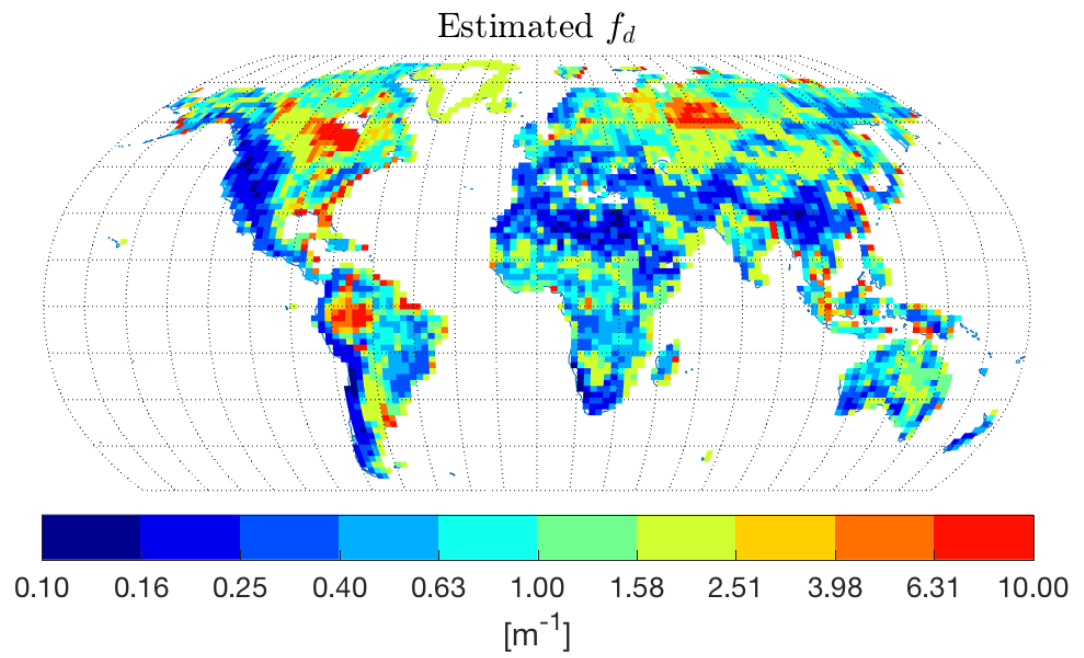
615 **Figure 3. Transient liquid pressure (a) and soil saturation (b) simulated by**
 616 **VSFM (solid line) and PFLOTRAN (square) for the water table dynamics test**
 617 **problem.**



618

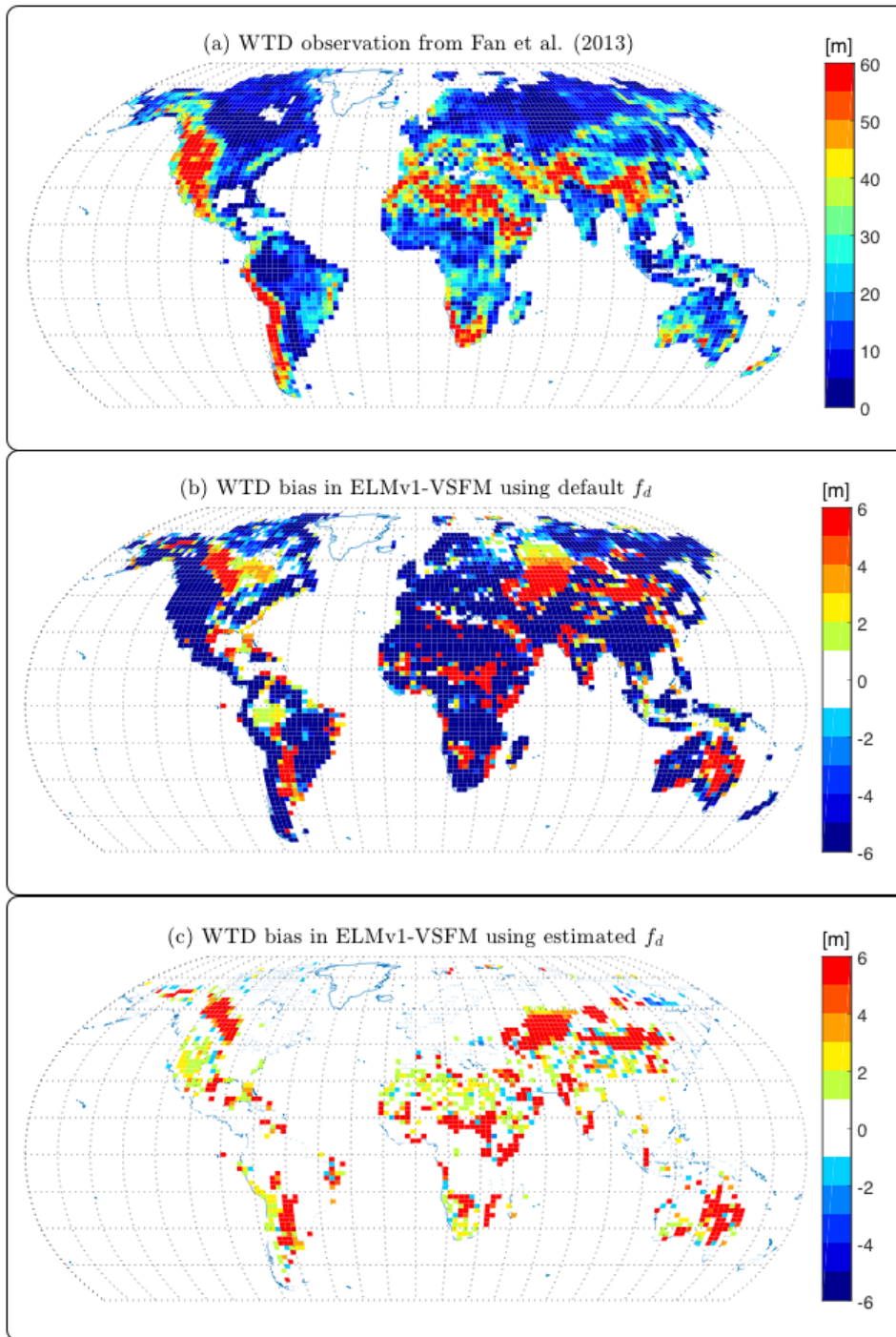
619 **Figure 4. (a-b) The nonlinear relationship between simulated water table**
 620 **depth (WTD) and f_d for two gridcells within ELM's global grid. WTD from the**
 621 **Fan et al. (2013) dataset and optimal f_d for the two gridcells are shown with a**
 622 **dashed red and dashed black lines, respectively. (c-d) The simulated drainage,**
 623 **evapotranspiration, and infiltration fluxes as functions of optimal f_d for the**
 624 **two ELM gridcells.**

625



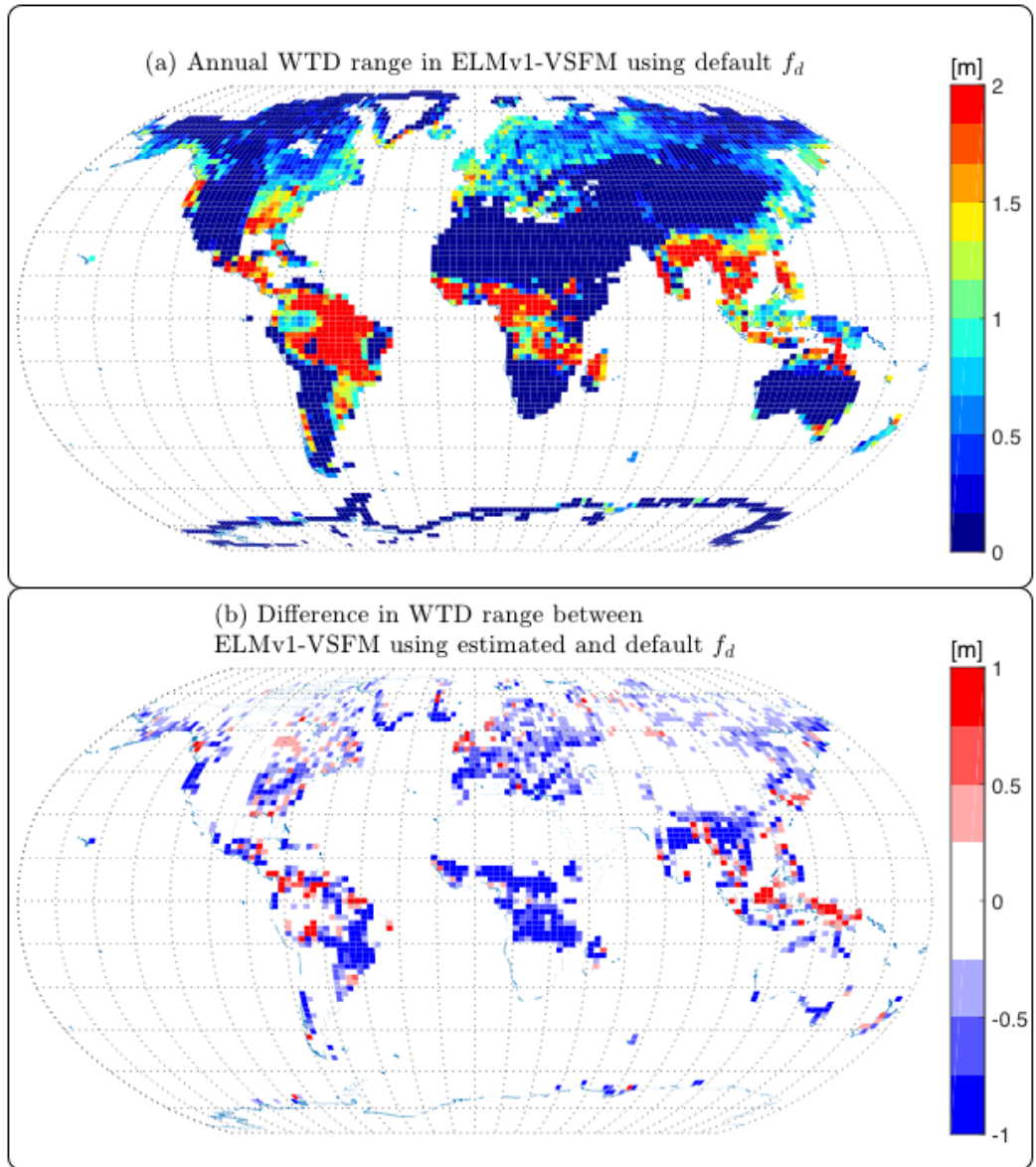
626

627 **Figure 5. Global estimate of f_d .**



628

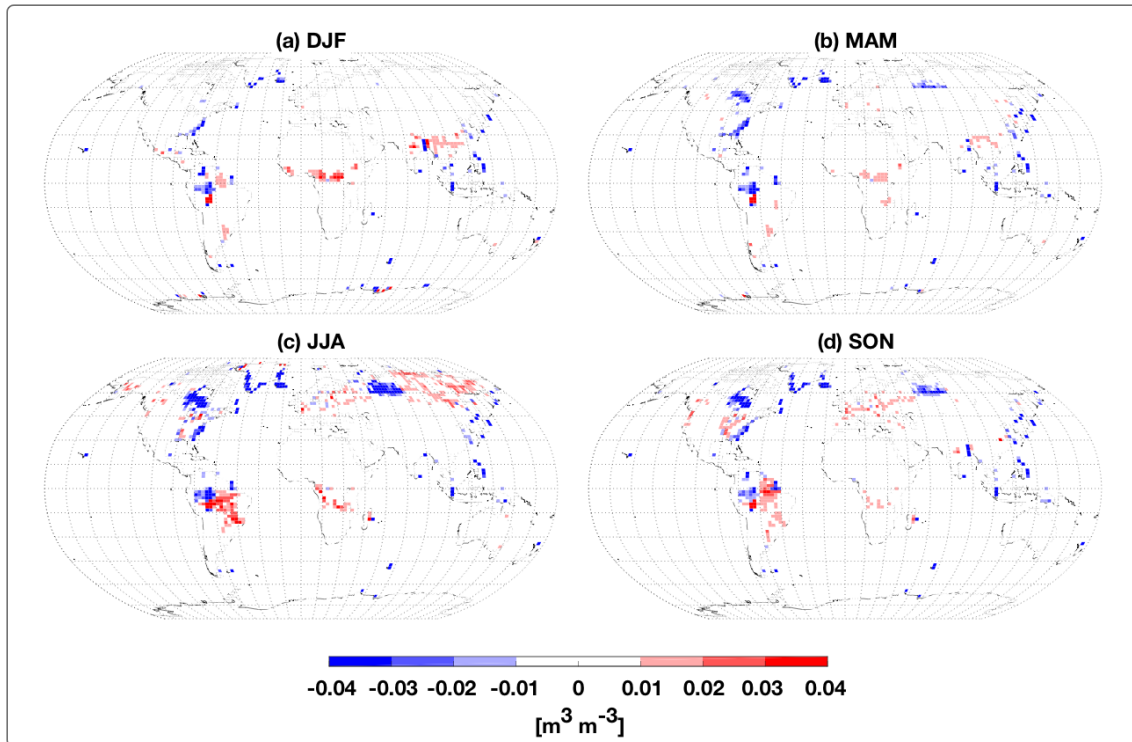
629 **Figure 6. (a) Water table depth observation from Fan et al. (2013); (b) Water**
 630 **table depth biases (=Model - Obs) from ELMv1-VSFM using default spatially**
 631 **homogeneous f_d ; and (c) Water table depth biases from ELMv1-VSFM using**
 632 **spatially heterogeneous f_d .**



634

635 **Figure 7. (a) Annual range of water table depth for ELMv1-VSFM simulation**636 **with spatially heterogeneous estimates of f_d and (b) Difference in annual**637 **water table depth range between simulations with optimal and default f_d .**

638



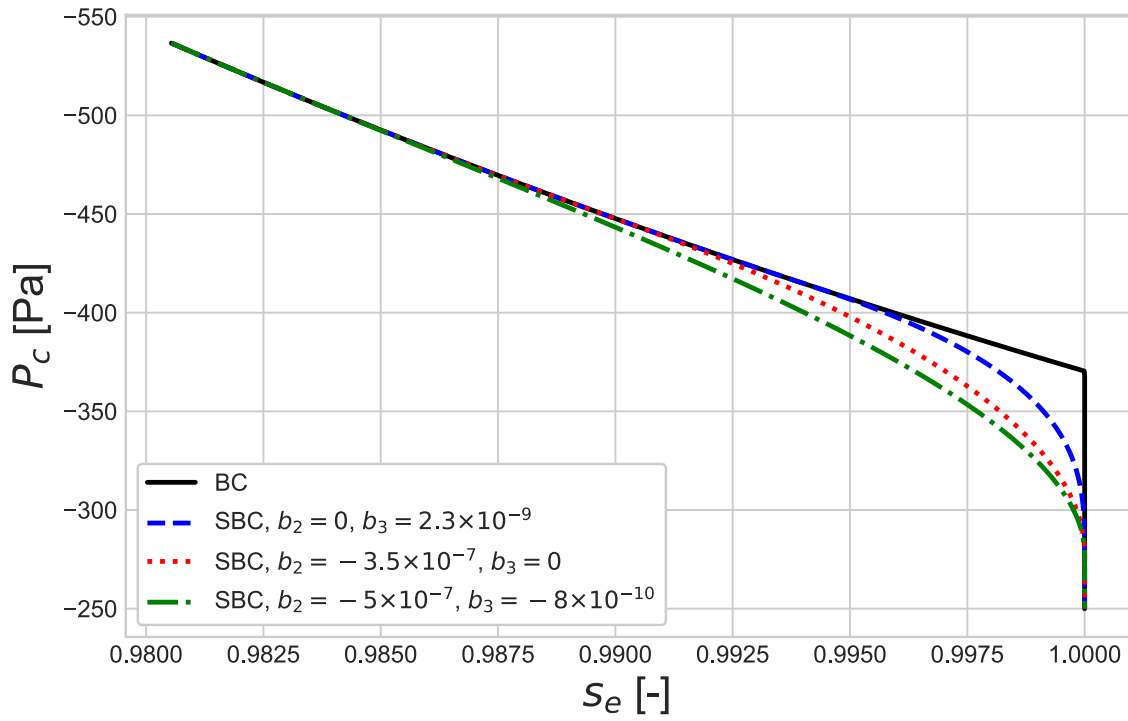
639

640 **Figure 8. Seasonal monthly mean soil moisture differences for top 10 cm**

641 **between ELMv1-VSFM simulations with optimal and default f_d values.**

642

643



644

645 **Figure A 1** The Brooks-Corey water rendition curve for estimating liquid saturation, s_e ,
646 as a function of capillary pressure, P_c , shown in solid black line and smooth
647 approximation of Brooks-Corey (SBC) are shown in dashed line.

648

649 **References**

- 650 Alkhaier, F., Flerchinger, G. N., and Su, Z.: Shallow groundwater effect on land surface
651 temperature and surface energy balance under bare soil conditions: modeling and
652 description, *Hydrol. Earth Syst. Sci.*, 16, 1817-1831, 2012.
- 653 Alley, W. M.: *Ground Water and Climate*, *Ground Water*, 39, 161-161, 2001.
- 654 Amenu, G. G. and Kumar, P.: A model for hydraulic redistribution incorporating
655 coupled soil-root moisture transport, *Hydrol. Earth Syst. Sci.*, 12, 55-74, 2008.
- 656 Anyah, R. O., Weaver, C. P., Miguez-Macho, G., Fan, Y., and Robock, A.: Incorporating
657 water table dynamics in climate modeling: 3. Simulated groundwater influence on
658 coupled land-atmosphere variability, *Journal of Geophysical Research: Atmospheres*,
659 113, n/a-n/a, 2008.
- 660 Balay, S., Abhyankar, S., Adams, M. F., Brown, J., Brune, P., Buschelman, K., Dalcin, L.,
661 Eijkhout, V., Gropp, W. D., Kaushik, D., Knepley, M. G., McInnes, L. C., Rupp, K., Smith,
662 B. F., Zampini, S., Zhang, H., and Zhang, H.: *PETSc Users Manual*, Argonne National
663 Laboratory ANL-95/11 - Revision 3.7, 1-241 pp., 2016.
- 664 Banks, E. W., Brunner, P., and Simmons, C. T.: Vegetation controls on variably
665 saturated processes between surface water and groundwater and their impact on the
666 state of connection, *Water Resources Research*, 47, n/a-n/a, 2011.
- 667 Bense, V. F., Kooi, H., Ferguson, G., and Read, T.: Permafrost degradation as a control
668 on hydrogeological regime shifts in a warming climate, *Journal of Geophysical
669 Research: Earth Surface*, 117, 2012.
- 670 Bernhardt, M., Schulz, K., Liston, G. E., and Zängl, G.: The influence of lateral snow
671 redistribution processes on snow melt and sublimation in alpine regions, *Journal of
672 Hydrology*, 424-425, 196-206, 2012.
- 673 Beven, K. J. and Kirkby, M. J.: A physically based, variable contributing area model of
674 basin hydrology / Un modèle à base physique de zone d'appel variable de l'hydrologie
675 du bassin versant, *Hydrological Sciences Bulletin*, 24, 43-69, 1979.
- 676 Bisht, G., Huang, M., Zhou, T., Chen, X., Dai, H., Hammond, G. E., Riley, W. J., Downs, J. L.,
677 Liu, Y., and Zachara, J. M.: Coupling a three-dimensional subsurface flow and transport
678 model with a land surface model to simulate stream-aquifer-land interactions
679 (CP v1.0), *Geosci. Model Dev.*, 10, 4539-4562, 2017.
- 680 Bisht, G., Riley, W. J., Wainwright, H. M., Dafflon, B., Yuan, F., and Romanovsky, V. E.:
681 Impacts of microtopographic snow redistribution and lateral subsurface processes
682 on hydrologic and thermal states in an Arctic polygonal ground ecosystem: a case
683 study using ELM-3D v1.0, *Geosci. Model Dev.*, 11, 61-76, 2018.
- 684 Bohrer, G., Mourad, H., Laursen, T. A., Drewry, D., Avissar, R., Poggi, D., Oren, R., and
685 Katul, G. G.: Finite element tree crown hydrodynamics model (FETCH) using porous
686 media flow within branching elements: A new representation of tree hydrodynamics,
687 *Water Resources Research*, 41, n/a-n/a, 2005.
- 688 Brooks, R. H. and Corey, A. T.: *Hydraulic properties of porous media*, Colorado State
689 University, Fort Collins, CO, 1964.
- 690 Brown, J., Knepley, M. G., May, D. A., McInnes, L. C., and Smith, B.: Composable linear
691 solvers for multiphysics, 2012, 55-62.
- 692 Brunke, M. A., Broxton, P., Pelletier, J., Gochis, D., Hazenberg, P., Lawrence, D. M.,
693 Leung, L. R., Niu, G.-Y., Troch, P. A., and Zeng, X.: Implementing and Evaluating Variable

694 Soil Thickness in the Community Land Model, Version 4.5 (CLM4.5), *Journal of*
695 *Climate*, 29, 3441-3461, 2016.

696 Celia, M. A., Bouloutas, E. T., and Zarba, R. L.: A general mass-conservative numerical
697 solution for the unsaturated flow equation, *Water Resources Research*, 26, 1483-
698 1496, 1990.

699 Chen, J. and Kumar, P.: Topographic Influence on the Seasonal and Interannual
700 Variation of Water and Energy Balance of Basins in North America, *Journal of Climate*,
701 14, 1989-2014, 2001.

702 Chen, X. and Hu, Q.: Groundwater influences on soil moisture and surface evaporation,
703 *Journal of Hydrology*, 297, 285-300, 2004.

704 Chen, Y., Chen, Y., Xu, C., Ye, Z., Li, Z., Zhu, C., and Ma, X.: Effects of ecological water
705 conveyance on groundwater dynamics and riparian vegetation in the lower reaches
706 of Tarim River, China, *Hydrological Processes*, 24, 170-177, 2010.

707 Clapp, R. B. and Hornberger, G. M.: Empirical equations for some soil hydraulic
708 properties, *Water Resources Research*, 14, 601-604, 1978.

709 Clark, M. P., Fan, Y., Lawrence, D. M., Adam, J. C., Bolster, D., Gochis, D. J., Hooper, R. P.,
710 Kumar, M., Leung, L. R., Mackay, D. S., Maxwell, R. M., Shen, C., Swenson, S. C., and Zeng,
711 X.: Improving the representation of hydrologic processes in Earth System Models,
712 *Water Resources Research*, 51, 5929-5956, 2015.

713 Collier, N., Hoffman, F. M., Lawrence, D. M., Keppel-Aleks, G., Koven, C. D., Riley, W.
714 J., Mu, M., and Randerson, J. T.: The International Land 1 Model Benchmarking
715 (ILAMB) System: Design, Theory, and Implementation, in review *J. Advances in*
716 *Modeling Earth Systems*, 2018. 2018.

717 Dai, A. and Trenberth, K. E.: Estimates of Freshwater Discharge from Continents:
718 Latitudinal and Seasonal Variations, *Journal of Hydrometeorology*, 3, 660-687, 2002.

719 Dams, J., Woldeamlak, S. T., and Batelaan, O.: Predicting land-use change and its
720 impact on the groundwater system of the Kleine Nete catchment, Belgium, *Hydrol.*
721 *Earth Syst. Sci.*, 12, 1369-1385, 2008.

722 Dennis, J. M., Vertenstein, M., Worley, P. H., Mirin, A. A., Craig, A. P., Jacob, R., and
723 Mickelson, S.: Computational performance of ultra-high-resolution capability in the
724 Community Earth System Model, *The International Journal of High Performance*
725 *Computing Applications*, 26, 5-16, 2012.

726 E3SM Project, D.: Energy Exascale Earth System Model. 2018.

727 Fan, Y., Li, H., and Miguez-Macho, G.: Global Patterns of Groundwater Table Depth,
728 *Science*, 339, 940-943, 2013.

729 Fan, Y., Miguez-Macho, G., Weaver, C. P., Walko, R., and Robock, A.: Incorporating
730 water table dynamics in climate modeling: 1. Water table observations and
731 equilibrium water table simulations, *Journal of Geophysical Research: Atmospheres*,
732 112, n/a-n/a, 2007.

733 Farthing, M. W., Kees, C. E., and Miller, C. T.: Mixed finite element methods and higher
734 order temporal approximations for variably saturated groundwater flow, *Advances*
735 *in Water Resources*, 26, 373-394, 2003.

736 Ferguson, I. M. and Maxwell, R. M.: Human impacts on terrestrial hydrology: climate
737 change versus pumping and irrigation, *Environmental Research Letters*, 7, 044022,
738 2012.

739 Frampton, A., Painter, S., Lyon, S. W., and Destouni, G.: Non-isothermal, three-phase
740 simulations of near-surface flows in a model permafrost system under seasonal
741 variability and climate change, *Journal of Hydrology*, 403, 352-359, 2011.

742 Ghimire, B., Riley, W. J., Koven, C. D., Mu, M., and Randerson, J. T.: Representing leaf
743 and root physiological traits in CLM improves global carbon and nitrogen cycling
744 predictions, *Journal of Advances in Modeling Earth Systems*, 8, 598-613, 2016.

745 Grant, R. F., Humphreys, E. R., and Lafleur, P. M.: Ecosystem CO₂ and CH₄ exchange in
746 a mixed tundra and a fen within a hydrologically diverse Arctic landscape: 1. Modeling
747 versus measurements, *Journal of Geophysical Research: Biogeosciences*, 120, 1366-
748 1387, 2015.

749 Grant, R. F., Mekonnen, Z. A., Riley, W. J., Wainwright, H. M., Graham, D., and Torn, M.
750 S.: Mathematical Modelling of Arctic Polygonal Tundra with Ecosys: 1.
751 Microtopography Determines How Active Layer Depths Respond to Changes in
752 Temperature and Precipitation, *Journal of Geophysical Research: Biogeosciences*,
753 122, 3161-3173, 2017.

754 Green, T. R., Taniguchi, M., Kooi, H., Gurdak, J. J., Allen, D. M., Hiscock, K. M., Treidel, H.,
755 and Aureli, A.: Beneath the surface of global change: Impacts of climate change on
756 groundwater, *Journal of Hydrology*, 405, 532-560, 2011.

757 Gutmann, E. D. and Small, E. E.: The effect of soil hydraulic properties vs. soil texture
758 in land surface models, *Geophysical Research Letters*, 32, 2005.

759 Hammond, G. E. and Lichtner, P. C.: Field-scale model for the natural attenuation of
760 uranium at the Hanford 300 Area using high-performance computing, *Water*
761 *Resources Research*, 46, n/a-n/a, 2010.

762 Hilberts, A. G. J., Troch, P. A., and Paniconi, C.: Storage-dependent drainable porosity
763 for complex hillslopes, *Water Resources Research*, 41, n/a-n/a, 2005.

764 Hoffman, F. M., Koven, C. D., Keppel-Aleks, G., Lawrence, D. M., Riley, W. J., Randerson,
765 J. T., Ahlstrom, A., Abramowitz, G., Baldocchi, D. D., Best, M. J., Bond-Lamberty, B.,
766 Kauwe}, M. G. D., Denning, A. S., Desai, A. R., Eyring, V., Fisher, J. B., Fisher, R. A.,
767 Gleckler, P. J., Huang, M., Hugelius, G., Jain, A. K., Kiang, N. Y., Kim, H., Koster, R. D.,
768 Kumar, S. V., Li, H., Luo, Y., Mao, J., McDowell, N. G., Mishra, U., Moorcroft, P. R., Pau, G.
769 S. H., Ricciuto, D. M., Schaefer, K., Schwalm, C. R., Serbin, S. P., Shevliakova, E., Slater,
770 A. G., Tang, J., Williams, M., Xia, J., Xu, C., Joseph, R., and Koch, D.: International Land
771 Model Benchmarking (ILAMB) 2016 Workshop Report, U.S. Department of Energy,
772 Office of Science, 159 pp., 2017.

773 Hou, Z., Huang, M., Leung, L. R., Lin, G., and Ricciuto, D. M.: Sensitivity of surface flux
774 simulations to hydrologic parameters based on an uncertainty quantification
775 framework applied to the Community Land Model, *Journal of Geophysical Research:*
776 *Atmospheres*, 117, n/a-n/a, 2012.

777 Hwang, T., Band, L. E., Vose, J. M., and Tague, C.: Ecosystem processes at the watershed
778 scale: Hydrologic vegetation gradient as an indicator for lateral hydrologic
779 connectivity of headwater catchments, *Water Resources Research*, 48, n/a-n/a, 2012.

780 Ji, P., Yuan, X., and Liang, X.-Z.: Do Lateral Flows Matter for the Hyperresolution Land
781 Surface Modeling?, *Journal of Geophysical Research: Atmospheres*, doi:
782 10.1002/2017JD027366, 2017. n/a-n/a, 2017.

783 Jiang, X., Niu, G.-Y., and Yang, Z.-L.: Impacts of vegetation and groundwater dynamics
784 on warm season precipitation over the Central United States, *Journal of Geophysical*
785 *Research: Atmospheres*, 114, n/a-n/a, 2009.

786 Jung, M., Reichstein, M., and Bondeau, A.: Towards global empirical upscaling of
787 FLUXNET eddy covariance observations: validation of a model tree ensemble
788 approach using a biosphere model, *Biogeosciences*, 6, 2001-2013, 2009.

789 Kane, D. L., Hinkel, K. M., Goering, D. J., Hinzman, L. D., and Outcalt, S. I.: Non-
790 conductive heat transfer associated with frozen soils, *Global and Planetary Change*,
791 29, 275-292, 2001.

792 Kees, C. E. and Miller, C. T.: Higher order time integration methods for two-phase flow,
793 *Advances in Water Resources*, 25, 159-177, 2002.

794 Kim, H., Yeh, P. J. F., Oki, T., and Kanae, S.: Role of rivers in the seasonal variations of
795 terrestrial water storage over global basins, *Geophysical Research Letters*, 36, n/a-
796 n/a, 2009.

797 Kollet, S. J. and Maxwell, R. M.: Capturing the influence of groundwater dynamics on
798 land surface processes using an integrated, distributed watershed model, *Water*
799 *Resources Research*, 44, n/a-n/a, 2008.

800 Koster, R. D., Suarez, M. J., Ducharne, A., Stieglitz, M., and Kumar, P.: A catchment-
801 based approach to modeling land surface processes in a general circulation model: 1.
802 Model structure, *Journal of Geophysical Research: Atmospheres*, 105, 24809-24822,
803 2000.

804 Kundzewicz, Z. W. and Doli, P.: Will groundwater ease freshwater stress under climate
805 change?, *Hydrological Sciences Journal*, 54, 665-675, 2009.

806 Lasslop, G., Reichstein, M., Papale, D., Richardson, A. D., Arneth, A., Barr, A., Stoy, P.,
807 and Wohlfahrt, G.: Separation of net ecosystem exchange into assimilation and
808 respiration using a light response curve approach: critical issues and global
809 evaluation, *Global Change Biology*, 16, 187-208, 2010.

810 Leng, G., Huang, M., Tang, Q., and Leung, L. R.: A modeling study of irrigation effects
811 on global surface water and groundwater resources under a changing climate, *Journal*
812 *of Advances in Modeling Earth Systems*, 7, 1285-1304, 2015.

813 Leng, G., Leung, L. R., and Huang, M.: Significant impacts of irrigation water sources
814 and methods on modeling irrigation effects in the ACMEland Model, *Journal of*
815 *Advances in Modeling Earth Systems*, 9, 1665-1683, 2017.

816 Leung, L. R., Huang, M., Qian, Y., and Liang, X.: Climate-soil-vegetation control on
817 groundwater table dynamics and its feedbacks in a climate model, *Climate Dynamics*,
818 36, 57-81, 2011.

819 Levine, J. B. and Salvucci, G. D.: Equilibrium analysis of groundwater-vadose zone
820 interactions and the resulting spatial distribution of hydrologic fluxes across a
821 Canadian Prairie, *Water Resources Research*, 35, 1369-1383, 1999.

822 Liang, X., Xie, Z., and Huang, M.: A new parameterization for surface and groundwater
823 interactions and its impact on water budgets with the variable infiltration capacity
824 (VIC) land surface model, *Journal of Geophysical Research: Atmospheres*, 108, n/a-
825 n/a, 2003.

826 Lohse, K. A., Brooks, P. D., McIntosh, J. C., Meixner, T., and Huxman, T. E.: Interactions
827 Between Biogeochemistry and Hydrologic Systems, *Annual Review of Environment*
828 *and Resources*, 34, 65-96, 2009.

829 Manoli, G., Bonetti, S., Domec, J.-C., Putti, M., Katul, G., and Marani, M.: Tree root
830 systems competing for soil moisture in a 3D soil–plant model, *Advances in Water*
831 *Resources*, 66, 32-42, 2014.

832 Marvel, K., Biasutti, M., Bonfils, C., Taylor, K. E., Kushnir, Y., and Cook, B. I.: Observed
833 and Projected Changes to the Precipitation Annual Cycle, *Journal of Climate*, 30, 4983-
834 4995, 2017.

835 Maxwell, R. M. and Miller, N. L.: Development of a Coupled Land Surface and
836 Groundwater Model, *Journal of Hydrometeorology*, 6, 233-247, 2005.

837 McDowell, N. G. and Allen, C. D.: Darcy's law predicts widespread forest mortality
838 under climate warming, *Nature Clim. Change*, 5, 669-672, 2015.

839 Miguez-Macho, G., Fan, Y., Weaver, C. P., Walko, R., and Robock, A.: Incorporating
840 water table dynamics in climate modeling: 2. Formulation, validation, and soil
841 moisture simulation, *Journal of Geophysical Research: Atmospheres*, 112, n/a-n/a,
842 2007.

843 Milly, P. C. D., Malyshev, S. L., Shevliakova, E., Dunne, K. A., Findell, K. L., Gleeson, T.,
844 Liang, Z., Philipps, P., Stouffer, R. J., and Swenson, S.: An Enhanced Model of Land
845 Water and Energy for Global Hydrologic and Earth-System Studies, *Journal of*
846 *Hydrometeorology*, 15, 1739-1761, 2014.

847 Mualem, Y.: A new model for predicting the hydraulic conductivity of unsaturated
848 porous media, *Water Resources Research*, 12, 513-522, 1976.

849 Niu, G.-Y., Yang, Z.-L., Dickinson, R. E., and Gulden, L. E.: A simple TOPMODEL-based
850 runoff parameterization (SIMTOP) for use in global climate models, *Journal of*
851 *Geophysical Research: Atmospheres*, 110, n/a-n/a, 2005.

852 Niu, G.-Y., Yang, Z.-L., Dickinson, R. E., Gulden, L. E., and Su, H.: Development of a simple
853 groundwater model for use in climate models and evaluation with Gravity Recovery
854 and Climate Experiment data, *Journal of Geophysical Research: Atmospheres*, 112,
855 n/a-n/a, 2007.

856 Niu, J., Shen, C., Chambers, J. Q., Melack, J. M., and Riley, W. J.: Interannual Variation in
857 Hydrologic Budgets in an Amazonian Watershed with a Coupled Subsurface–Land
858 Surface Process Model, *Journal of Hydrometeorology*, 18, 2597-2617, 2017.

859 Oleson, K. W., D.M. Lawrence, G.B. Bonan, B. Drewniak, M. Huang, C.D. Koven, S. Levis,
860 F. Li, W.J. Riley, Z.M. Subin, S.C. Swenson, P.E. Thornton, A. Bozbiyik, R. Fisher, E.
861 Kluzek, J.-F. Lamarque, P.J. Lawrence, L.R. Leung, W. Lipscomb, S. Muszala, D.M.
862 Ricciuto, W. Sacks, Y. Sun, J. Tang, Z.-L. Yang: Technical Description of version 4.5 of
863 the Community Land Model (CLM), National Center for Atmospheric Research,
864 Boulder, CO, 422 pp., 2013.

865 Pacific, V. J., McGlynn, B. L., Riveros-Iregui, D. A., Welsch, D. L., and Epstein, H. E.:
866 Landscape structure, groundwater dynamics, and soil water content influence soil
867 respiration across riparian–hillslope transitions in the Tenderfoot Creek
868 Experimental Forest, Montana, *Hydrological Processes*, 25, 811-827, 2011.

869 Pelletier, J. D., Broxton, P. D., Hazenberg, P., Zeng, X., Troch, P. A., Niu, G.-Y., Williams,
870 Z., Brunke, M. A., and Gochis, D.: A gridded global data set of soil, intact regolith, and
871 sedimentary deposit thicknesses for regional and global land surface modeling,
872 *Journal of Advances in Modeling Earth Systems*, 8, 41-65, 2016.

873 Petra, D.: Vulnerability to the impact of climate change on renewable groundwater
874 resources: a global-scale assessment, *Environmental Research Letters*, 4, 035006,
875 2009.

876 Piao, S. L., Ito, A., Li, S. G., Huang, Y., Ciais, P., Wang, X. H., Peng, S. S., Nan, H. J., Zhao, C.,
877 Ahlström, A., Andres, R. J., Chevallier, F., Fang, J. Y., Hartmann, J., Huntingford, C., Jeong,
878 S., Levis, S., Levy, P. E., Li, J. S., Lomas, M. R., Mao, J. F., Mayorga, E., Mohammat, A.,
879 Muraoka, H., Peng, C. H., Peylin, P., Poulter, B., Shen, Z. H., Shi, X., Sitch, S., Tao, S., Tian,
880 H. Q., Wu, X. P., Xu, M., Yu, G. R., Viovy, N., Zaehle, S., Zeng, N., and Zhu, B.: The carbon
881 budget of terrestrial ecosystems in East Asia over the last two decades,
882 *Biogeosciences*, 9, 3571-3586, 2012.

883 Pruess, K., Oldenburg, C., and Moridis, G.: TOUGH2 User's Guide, Version 2.0,
884 Lawrence Berkeley National Laboratory, Berkeley, CALBNL-43134, 1999.

885 Rihani, J. F., Maxwell, R. M., and Chow, F. K.: Coupling groundwater and land surface
886 processes: Idealized simulations to identify effects of terrain and subsurface
887 heterogeneity on land surface energy fluxes, *Water Resources Research*, 46, n/a-n/a,
888 2010.

889 Salvucci, G. D. and Entekhabi, D.: Hillslope and Climatic Controls on Hydrologic Fluxes,
890 *Water Resources Research*, 31, 1725-1739, 1995.

891 Shen, C., Niu, J., and Phanikumar, M. S.: Evaluating controls on coupled hydrologic and
892 vegetation dynamics in a humid continental climate watershed using a subsurface-
893 land surface processes model, *Water Resources Research*, 49, 2552-2572, 2013.

894 Siebert, S., Burke, J., Faures, J. M., Frenken, K., Hoogeveen, J., Döll, P., and Portmann, F.
895 T.: Groundwater use for irrigation – a global inventory, *Hydrol. Earth Syst. Sci.*, 14,
896 1863-1880, 2010.

897 Sivapalan, M., Beven, K., and Wood, E. F.: On hydrologic similarity: 2. A scaled model
898 of storm runoff production, *Water Resources Research*, 23, 2266-2278, 1987.

899 Soylu, M. E., Istanbuluoglu, E., Lenters, J. D., and Wang, T.: Quantifying the impact of
900 groundwater depth on evapotranspiration in a semi-arid grassland region, *Hydrol.*
901 *Earth Syst. Sci.*, 15, 787-806, 2011.

902 Sperry, J. S., Adler, F. R., Campbell, G. S., and Comstock, J. P.: Limitation of plant water
903 use by rhizosphere and xylem conductance: results from a model, *Plant, Cell &*
904 *Environment*, 21, 347-359, 1998.

905 Srivastava, R. and Yeh, T. C. J.: Analytical solutions for one-dimensional, transient
906 infiltration toward the water table in homogeneous and layered soils, *Water*
907 *Resources Research*, 27, 753-762, 1991.

908 Swenson, S. C. and Lawrence, D. M.: Assessing a dry surface layer-based soil resistance
909 parameterization for the Community Land Model using GRACE and FLUXNET-MTE
910 data, *Journal of Geophysical Research: Atmospheres*, 119, 10,299-210,312, 2014.

911 Swenson, S. C., Lawrence, D. M., and Lee, H.: Improved simulation of the terrestrial
912 hydrological cycle in permafrost regions by the Community Land Model, *Journal of*
913 *Advances in Modeling Earth Systems*, 4, n/a-n/a, 2012.

914 Tanaka, M., Girard, G., Davis, R., Peuto, A., and Bignell, N.: Recommended table for the
915 density of water between 0 °C and 40 °C based on recent experimental reports,
916 *Metrologia*, 38, 301, 2001.

917 Taylor, K. E., Stouffer, R. J., and Meehl, G. A.: An Overview of CMIP5 and the Experiment
918 Design, *Bulletin of the American Meteorological Society*, 93, 485-498, 2012.

919 Taylor, R. G., Scanlon, B., Döll, P., Rodell, M., Van Beek, R., Wada, Y., Longuevergne, L.,
920 Leblanc, M., Famiglietti, J. S., and Edmunds, M.: Ground water and climate change,
921 Nature Climate Change, 3, 322-329, 2013.

922 Tian, W., Li, X., Cheng, G. D., Wang, X. S., and Hu, B. X.: Coupling a groundwater model
923 with a land surface model to improve water and energy cycle simulation, Hydrol.
924 Earth Syst. Sci., 16, 4707-4723, 2012.

925 van Genuchten, M. T.: A Closed-form Equation for Predicting the Hydraulic
926 Conductivity of Unsaturated Soils¹, Soil Science Society of America Journal, 44, 892-
927 898, 1980.

928 Walko, R. L., Band, L. E., Baron, J., Kittel, T. G. F., Lammers, R., Lee, T. J., Ojima, D., Sr., R.
929 A. P., Taylor, C., Tague, C., Tremback, C. J., and Vidale, P. L.: Coupled Atmosphere-
930 Biophysics-Hydrology Models for Environmental Modeling, Journal of Applied
931 Meteorology, 39, 931-944, 2000.

932 White, M. and STOMP, O. M.: Subsurface transport over multiple phases; Version 2.0;
933 Theory Guide, Pacific Northwest National Laboratory, 2000. 2000.

934 Yeh, P. J.-F. and Eltahir, E. A. B.: Representation of Water Table Dynamics in a Land
935 Surface Scheme. Part I: Model Development, Journal of Climate, 18, 1861-1880, 2005.

936 York, J. P., Person, M., Gutowski, W. J., and Winter, T. C.: Putting aquifers into
937 atmospheric simulation models: an example from the Mill Creek Watershed,
938 northeastern Kansas, Advances in Water Resources, 25, 221-238, 2002.

939 Yuan, X., Xie, Z., Zheng, J., Tian, X., and Yang, Z.: Effects of water table dynamics on
940 regional climate: A case study over east Asian monsoon area, Journal of Geophysical
941 Research: Atmospheres, 113, n/a-n/a, 2008.

942 Zektser, I. S. and Evertt, L. G.: Groundwater resources of the world and their use,
943 United Nations Educational, Scientific and Cultural Organization⁷, place de Fontenoy,
944 75352 Paris 07 SP, 2004.

945 Zeng, X. and Decker, M.: Improving the Numerical Solution of Soil Moisture-Based
946 Richards Equation for Land Models with a Deep or Shallow Water Table, Journal of
947 Hydrometeorology, 10, 308-319, 2009.

948 Zhu, Q., Riley, W. J., Tang, J., and Koven, C. D.: Multiple soil nutrient competition
949 between plants, microbes, and mineral surfaces: model development,
950 parameterization, and example applications in several tropical forests,
951 Biogeosciences, 13, 341-363, 2016.

952

953